

# Is JPEG AI going to change image forensics?

Edoardo Daniele Cannas<sup>†</sup>, Sara Mandelli<sup>†</sup>, Nataša Popović<sup>†</sup>, Ayman Alkhateeb\*  
 Alessandro Gnutti\*, Paolo Bestagini<sup>†</sup>, Stefano Tubaro<sup>†</sup>  
<sup>†</sup> Politecnico di Milano, \* Università degli Studi di Brescia

## Abstract

In this paper, we investigate the counter-forensic effects of the new JPEG AI standard based on neural image compression, focusing on two critical areas: deepfake image detection and image splicing localization. Neural image compression leverages advanced neural network algorithms to achieve higher compression rates while maintaining image quality. However, it introduces artifacts that closely resemble those generated by image synthesis techniques and image splicing pipelines, complicating the work of researchers when discriminating pristine from manipulated content. We comprehensively analyze JPEG AI's counter-forensic effects through extensive experiments on several state-of-the-art detectors and datasets. Our results demonstrate a reduction in the performance of leading forensic detectors when analyzing content processed through JPEG AI. By exposing the vulnerabilities of the available forensic tools we aim to raise the urgent need for multimedia forensics researchers to include JPEG AI images in their experimental setups and develop robust forensic techniques to distinguish between neural compression artifacts and actual manipulations.

## 1. Introduction

Neural image compression is an emerging technology that leverages deep learning techniques to compress images more efficiently than traditional methods [46, 64–66, 84, 94]. This approach is needed to address the growing demand for high-quality image storage and transmission in an era of proliferating visual content. Neural image compression is gaining traction due to its ability to achieve superior compression rates while maintaining visual quality, making it an attractive solution for various applications [59].

JPEG AI is a new standard in image compression developed to harness Neural Networks (NNs)' power [3, 17]. Published as an International Standard on February 2025 [16], JPEG AI aims not only to achieve superior rate-distortion performance for enhanced visual quality but also to enable faster coding speeds and provide the flexibility to optimize human viewing and machine analysis [17, 51].

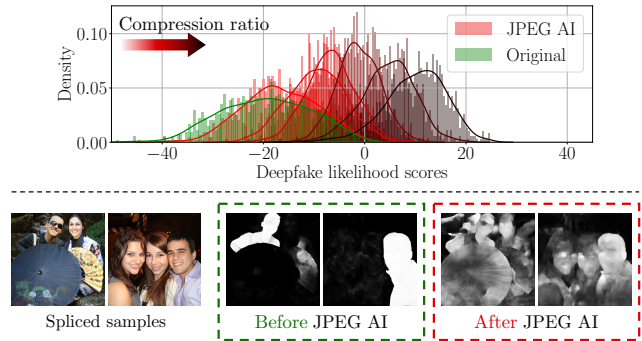


Figure 1. Main findings of our experimental campaign on the counter-forensic effect of JPEG AI. On the top row, we report the deepfake detection scores of pristine images and their JPEG AI-compressed versions as the compression ratio increases (darker red tones), proving that pristine images compressed with this new standard can be mistaken for deepfakes. On the bottom row, we show that, after JPEG AI compression, localization maps produced by state-of-the-art algorithms can no longer distinguish genuine from manipulated content.

However, the introduction of JPEG AI poses new challenges for image forensics [45]. JPEG AI, as a novel standard, introduces unique forensic footprints that require dedicated study to understand and exploit [22, 86]. Additionally, existing literature indicates that neural image compression schemes leave distinctive upsampling traces similar to those found in images generated by NNs, such as deepfakes [23]. Deepfake image detection is particularly active, with numerous contributions highlighting that NN-based image generation techniques leave artifacts due to upsampling operators [31, 40, 42, 63, 81, 88]. Furthermore, it is well-documented that locally manipulated (i.e., spliced) images may exhibit artifacts related to upsampling [80], too.

All these elements raise a significant issue: the potential for detectors to erroneously classify genuine content as malicious, either as deepfakes or locally manipulated images, due to the presence of JPEG AI compression traces. While the forensic literature is currently analyzing the implications of adopting JPEG AI, there are no general studies on its counter-forensic effects to our knowledge. Indeed, previous investigations have either focused on analyzing the

reconstruction artifacts left by neural compression methods [45] or the traces left by neural compression techniques that are practical for other forensic purposes [22, 23, 86]. Other contributions examined how image splicing detectors exploiting standard JPEG compression artifacts lower their performances whenever a user relies on neural compression [24] to save images.

This paper investigates whether state-of-the-art algorithms designed for deepfake image detection and image splicing localization can mistakenly identify JPEG AI-compressed images as malicious content. To achieve our goal, we consider several state-of-the-art detectors from both tasks. We first collect their test datasets and compress them using the official JPEG AI Reference Software [10]. Then, we evaluate if the detectors present a pronounced tendency to misclassify JPEG AI compressed samples as malicious, varying the compression ratio. We also examine the detector’s performance on images encoded with traditional JPEG compression, confirming that artifacts introduced by JPEG AI make detectors behave in a sort of opposite way to conventional compression methods. Finally, we preliminary show that incorporating JPEG AI images into the training pipeline of detectors may help mitigate this phenomenon, and also experiment with double JPEG AI compression.

The main findings of our experimental campaign are reported in Fig. 1. We prove that deepfake image detectors tend to classify images compressed with JPEG AI as synthetic samples (top row), while image splicing localization techniques risk being fooled by JPEG AI, as many missed detections and false alarms may arise in the estimated tampering masks (bottom row). All these effects prove to be stronger as the JPEG AI compression ratio increases.

In summary, the main contributions of our paper are: i) we are the first to investigate deepfake image detection and image splicing localization tasks focusing on the official implementation of JPEG AI; ii) despite the exceptional visual quality of JPEG AI images, we demonstrate that state-of-the-art detectors are misled by their interpolation artifacts; iii) we reveal that this effect is incomparable with standard compression formats like JPEG; iv) we introduce JPEG AI samples into training to reduce the effects of this phenomenon; v) we investigate the counter-forensic effects of double JPEG AI compression.

## 2. JPEG AI background

**General framework.** In February 2025, the JPEG Standardization Committee published JPEG AI as the first international image coding standard based on end-to-end learning [16]. The general architecture of JPEG AI is depicted in Fig. 2 [50]. The basic functioning follows the same of many other neural image compression algorithms: it first transforms an image into a latent tensor, which is then com-

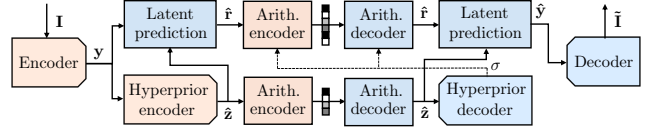


Figure 2. JPEG AI framework.

pressed and transmitted to the receiver, allowing the decoder to either reconstruct the image or carry out additional operations directly in the compressed domain exploiting the latent tensor [17]. The entire JPEG AI codec is trained end-to-end by minimizing a rate-distortion loss function. By adjusting the weight of the rate term, different models can be trained to achieve variable-rate compression, corresponding to various Bits Per Pixel (BPP). We refer the reader to the supplemental material, Sec. 7, for more details on each architectural module.

While many neural image compression techniques exist [67] (please refer to the supplemental material for more discussion), in our analysis we specifically focus on JPEG AI given its forthcoming impact. Indeed, JPEG AI presents interesting characteristics that are likely to spread its adoption among users, including support for a wide array of devices with different characteristics [16] and the direct involvement of technology companies [9].

It is noteworthy to mention that JPEG AI, as a standardized format, enforces strict compliance requirements on manufacturers, limiting customization options within the compression pipeline. In particular, the blue modules in Fig. 2, among which we can notice the decoder, are formally normative. This adherence to a fixed architecture suggests that images decoded with JPEG AI, even when produced by different manufacturers, will likely display similar characteristics and forensic artifacts.

**JPEG AI compression artifacts.** Recently, it has been shown that neural compression codecs can leave frequency artifacts similar to those of synthetic generation techniques [22, 23]. These artifacts presumably stem from the use of upsampling operators in the decoding process, and can be misleading for forensic detectors that rely on similar forensic footprints to accomplish their task. In this vein, we perform a similar analysis for JPEG AI compression, following a well-known forensic procedure, i.e., we compute the average Fourier spectrum of noise residuals extracted from images under analysis [32, 63].

The first row of Fig. 3 shows the average Fourier spectra of residuals computed from the JPEG AI versions of 10K images of the FFHQ dataset [54] (left block) and of 13.5K LSUN images [95] (right block). We consider BPP target values of 0.12, 0.25 and 0.5, as suggested by the JPEG AI Call For Evidence [1]. Interestingly, JPEG AI spectra present peaks that resemble those already noticed for synthetic images [32, 63], though being less pronounced. The peaks vary in intensity and frequency index according to the

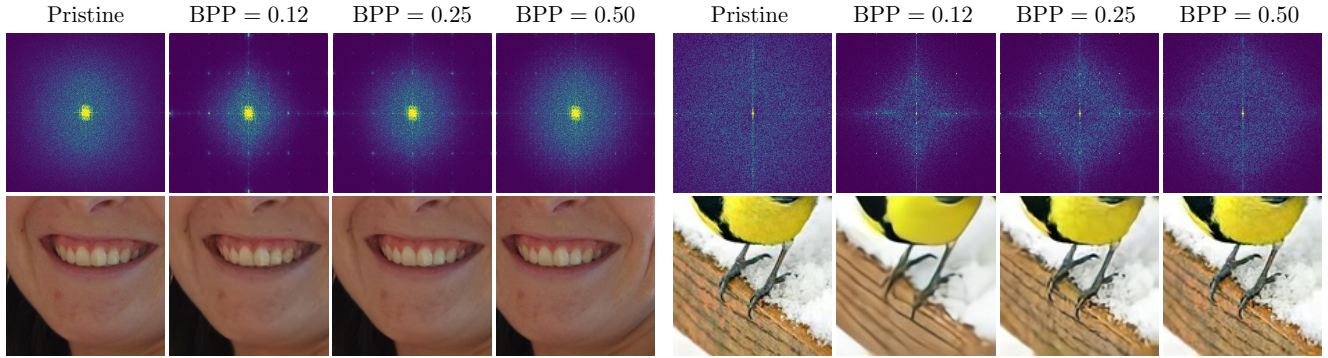


Figure 3. Example of JPEG AI artifacts left at different BPP values in the Fourier and spatial domains. Left block: FFHQ dataset; right block: LSUN dataset. In the first row, we show the average Fourier spectra (magnitude) of pristine and JPEG AI images; all spectra are centered in the spatial frequencies  $(0, 0)$ . In the second row, we show the close-up of one image per dataset. Best viewed in electronic format.

BPP used. These results drive us to our proposed analysis of the counter-forensic effects of JPEG AI.

Moreover, if LSUN samples compression at lower BPPs shows a prominent low-pass filtering effect, this behavior is much less pronounced on FFHQ. As an example, in the second row of Fig. 3, we report the close-up of one image per dataset. On FFHQ samples (left), few artifacts are visible on specific face regions that are well known to be hard to reconstruct by neural decoders, like teeth, eyes, and ears [87]. LSUN samples (right) look more low-pass filtered at low BPPs, even though 0.50 BPP are already enough to reconstruct high-frequency details.

### 3. Case studies

In this paper, we aim to verify if forensic detectors fail to work correctly when dealing with JPEG AI-compressed images. We focus mainly on two forensics tasks: i) deepfake image detection and ii) image splicing localization. In the following, we illustrate each of them and motivate our proposed experiments.

**Deepfake image detection.** With deepfake image detection, we refer to identifying images created through synthetic generation techniques, such as Generative Adversarial Networks (GANs) or diffusion models. Given an image  $\mathbf{I}$ , state-of-the-art detectors implement a binary classifier  $D(\cdot)$  returning a detection score  $s = D(\mathbf{I})$  for the image being a deepfake. Higher scores usually indicate a higher likelihood of the image being synthetically generated, with practitioners using a fixed threshold, e.g., 0, to separate the two classes (if the score is greater than 0, the image is classified as fake, otherwise it is detected as pristine).

Our study investigates whether state-of-the-art detectors produce high scores when processing images compressed with JPEG AI. We aim to check if the artifacts introduced by JPEG AI (like the ones previously shown in Sec. 2) are misinterpreted by these detectors leading to the misclassification of pristine samples as deepfakes or to alterations of the

scores of deepfake images. To do so, we compare the distributions of the scores obtained from JPEG AI-uncompressed images and their JPEG AI-compressed versions.

**Image splicing localization.** With image splicing localization, we refer to the pixel-level identification of local manipulations in an image. For instance, this general manipulation manifests in the so-called “Photoshopped” or “cheapfake” [71] pictures, i.e., images where a malicious actor altered some pixels by copying content from another picture. To assess the integrity of the image under analysis, state-of-the-art detectors output an estimated real-valued tampering mask  $\tilde{\mathbf{M}}$ , whose values indicate the likelihood of manipulation for each pixel. Similarly to deepfake image detection, imposing a threshold on the likelihood values generates a binary tampering mask that classifies each pixel as manipulated or genuine.

We aim to verify whether image splicing localization tools alter their output masks  $\tilde{\mathbf{M}}$  when the input samples are compressed with JPEG AI, i.e., we compare the masks  $\tilde{\mathbf{M}}$  obtained from spliced samples before and after JPEG AI compression. In particular, we check if manipulated pixels are still correctly reported in the final estimated binary mask, and we inspect if JPEG AI artifacts cause some pristine pixels to be incorrectly classified as manipulated.

## 4. Experimental setup

### 4.1. Deepfake image detection

**Forensic detectors.** To have an exhaustive picture of the effects of JPEG AI on deepfake image detection, we select several state-of-the-art detectors ranging from Convolutional Neural Networks (CNNs) to transformers-based architectures, trained with different paradigms on diverse datasets. In particular, we choose the detector proposed in [88], available in two variants, i.e., [88]-A and [88]-B, the detectors proposed in [32, 42, 63, 70, 81] and, finally, the two approaches presented in [34], i.e., [34]-A and [34]-

B. All these tools are publicly available, with both test code and model weights. We rely on the original authors’ implementation for each detector to execute our experiments<sup>1</sup>.

**Test set.** To avoid any possible bias due to data distribution mismatching, we test each detector on the same test set used by the original authors. Our experiments’ final set of images comprehends pristine samples from CelebA [61], COCO [60], FFHQ [54], Imagenet [37], LAION [78], LSUN [95], and RAISE [35] datasets. For every pristine test set, we include a deepfake counterpart, selected by the original authors to depict similar content to the pristine one<sup>1</sup>. We process all these images through JPEG AI compression, following a specific paradigm we detail in Sec. 4.3.

**Evaluation metrics.** To quantify the counter-forensic effects of JPEG AI, we compare pristine and deepfake scores’ distributions considering two scenarios, i.e., *before* and *after* JPEG AI compression is applied to our test images. Our goal is to quantify how much JPEG AI alters these scores’ distribution.

As previously conjectured, we expect JPEG AI to move the score distribution of pristine samples to the “deepfake” area, i.e., above the 0 threshold, potentially producing more false alarms. Moreover, we later show that JPEG AI compression does not only modify pristine samples’ distributions, but it can also affect those of synthetic images. To quantify these modifications, we use standard binary classification metrics, namely the Area Under the Curve (AUC), the Balanced Accuracy (BA), the False Positive Rate (FPR), and the False Negative Rate (FNR) evaluated at 0 threshold. The FPR quantifies the ratio of pristine samples misclassified as synthetic (i.e., the false alarms), while the FNR represents the ratio of synthetic samples misclassified as pristine. If the JPEG AI has no effect, these metrics should remain the same before and after the compression.

## 4.2. Image splicing localization

**Forensic detectors.** We focus on the latest and top-performing state-of-the-art techniques based on deep learning models. In particular, we choose three detectors: i) TruFor [43], a method based on a denoising CNN; ii) MMFusion [85], a framework for the multi-modal fusion of different image splicing localization techniques; iii) ImageForensicsOSN (IFOSN) [92], a technique robust to social network compression schemes. Code and model weights are available online, and we rely on the original author’s implementation for our experiments.

**Test set.** We consider standard benchmarks in the field, i.e., CASIA [39], Columbia [47], Coverage [91], COCOglide [43], and DSO-1 [28, 36]. All detectors were originally tested with excellent performances on these datasets, which comprise uncompressed samples (DSO-1,

Columbia, Coverage, COCOglide) and JPEG images (CASIA). We compress all these images through JPEG AI by following the specifications provided in Sec. 4.3.

**Evaluation metrics.** In this case as well, we evaluate the performances of all detectors on the JPEG AI-uncompressed version of the datasets and their JPEG AI-compressed version. In specific, we compare the ground truth mask  $M$  against the estimated real-valued mask  $\tilde{M}$  for each sample *before* and *after* the compression.

Without counter-forensic effects, we expect a correct separation between pristine and tampered with pixels. On the contrary, in the case of the counter-forensic effect of JPEG AI, we expect a potential performance drop since JPEG AI compression might hinder or introduce new artifacts. To measure this behavior, we consider standard metrics for the image splicing localization task, namely the pixel level AUC, the BA and the F1-score. The BA and the F1-score are evaluated at the 0.5 threshold.

## 4.3. Dataset compression

We compress the datasets illustrated above using the official JPEG AI Reference Software [10]. In particular, we use version 7.0 of the JPEG AI Verification Model [10] with the High Operation Point (HOP) configuration and enable all tools to achieve the best coding performance [10]. We rely on six different BPP values, i.e., 0.12, 0.25, 0.5, 0.75, 1.0, and 2.0. We select these values from the official target rates of the JPEG AI Call for Evidence Challenge [1]. With this approach, we have a believable overview of how the compression ratio affects the presence of artifacts and, in turn, the performance of forensic detectors.

## 5. Results

### 5.1. Deepfake image detection

**Preliminary analysis.** Before analyzing the counter-forensic effect of JPEG AI, we first evaluate the various detectors on pristine and synthetic images *not compressed with JPEG AI*. This approach allows us to verify if detectors achieve acceptable performances for the standard real-vs-deepfake task. The first column of Tab. 1 reports the results averaged across all datasets. On average, all detectors show satisfactory performances<sup>2</sup>.

Given our goal of studying the effect of JPEG AI on misleading deepfake image detectors, in the following, we discard results from datasets where detectors’ performances do not exceed an AUC of 0.75. Indeed, we want to analyze the counter-forensic effects of JPEG AI only when the initial dataset (*before* JPEG AI compression) is classified with acceptable performances by the detectors.

<sup>1</sup>Complete experimental details in the Supplementary Material Sec. 8. All code for replicating our experiments is available [here](#).

<sup>2</sup>Complete results for all detectors and all datasets are available in Sec. 9 and Sec. 10 of the Supplementary Material.

Table 1. BA, FPR, and FNR evaluated at 0 threshold for the deepfake image detection case study before and after JPEG AI compression.

	Original format			BPP = 0.12			BPP = 0.25			BPP = 0.5			BPP = 0.75			BPP = 1.0		
	BA $\uparrow$	FPR $\downarrow$	FNR $\downarrow$	BA $\uparrow$	FPR $\downarrow$	FNR $\downarrow$	BA $\uparrow$	FPR $\downarrow$	FNR $\downarrow$	BA $\uparrow$	FPR $\downarrow$	FNR $\downarrow$	BA $\uparrow$	FPR $\downarrow$	FNR $\downarrow$	BA $\uparrow$	FPR $\downarrow$	FNR $\downarrow$
[88]-A	0.82	0.04	0.31	0.62	0.56	0.20	0.71	0.35	0.22	0.76	0.16	0.32	0.80	0.09	0.32	0.79	0.06	0.36
[88]-B	0.74	0.01	0.51	0.64	0.16	0.56	0.69	0.06	0.57	0.71	0.02	0.56	0.73	0.01	0.53	0.73	0.01	0.53
[42]	0.72	0.03	0.54	0.50	0.96	0.04	0.52	0.86	0.11	0.72	0.38	0.18	0.72	0.22	0.33	0.76	0.08	0.41
[32]	0.77	0.00	0.46	0.50	0.97	0.02	0.59	0.52	0.29	0.65	0.03	0.66	0.67	0.01	0.66	0.69	0.00	0.63
[70]	0.91	0.02	0.15	0.71	0.42	0.17	0.80	0.19	0.21	0.84	0.08	0.24	0.86	0.05	0.22	0.87	0.04	0.21
[34]-A	0.77	0.29	0.16	0.59	0.71	0.11	0.60	0.66	0.14	0.60	0.64	0.17	0.64	0.56	0.16	0.65	0.54	0.17
[34]-B	0.74	0.30	0.23	0.60	0.72	0.07	0.63	0.65	0.09	0.64	0.61	0.11	0.67	0.54	0.13	0.68	0.51	0.14
[81]	0.92	0.13	0.02	0.50	0.99	0.00	0.51	0.99	0.00	0.51	0.98	0.00	0.51	0.98	0.00	0.51	0.97	0.00
[63]	0.84	0.16	0.15	0.50	0.96	0.05	0.53	0.78	0.15	0.58	0.61	0.22	0.67	0.41	0.24	0.71	0.32	0.26

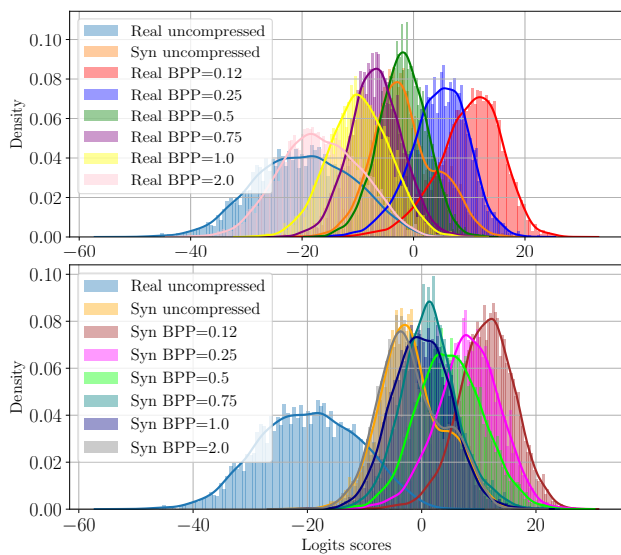


Figure 4. Scores distribution for [42] over COCO *pristine* samples (top row) and their *synthetic* counterpart samples (bottom row) compressed at different BPP values.

**Impact of compression ratio.** We begin our analysis by illustrating the effect of JPEG AI on the score distributions. Figure 4 depicts the logit scores distribution of detector [42] when processing original format and JPEG AI compressed samples from the COCO dataset<sup>2</sup>.

Interestingly, as the compression ratio increases (i.e., when we lower the BPPs), the distribution of the scores moves its center of gravity to the right (i.e., above the 0 threshold), almost independently from the class of the samples. This behavior has different implications. For pristine samples, we expect an increase in false positives. This right shift may cause fewer false negatives for deepfake samples instead.

To confirm this hypothesis quantitatively, Tab. 1 (starting from the second left column) reports the average results obtained by testing each detector on all its datasets<sup>3</sup>. For extremely low BPPs, all detectors exhibit a drop in the BA,

<sup>3</sup>We omit the AUC results and BPP= 2.0 scenario for clarity. Complete results are available in the Supplementary Material Sec. 9.

Table 2. JPEG AI MS-SSIM and VIF quality metrics.

BPP	0.12	0.25	0.5	0.75	1.0	2.0
MS-SSIM	0.97	0.98	0.99	1.00	1.00	1.00
VIF	38.15	40.28	42.47	44.33	45.89	48.08

especially for [32, 42, 63, 81], and they all experience an increase in the FPR. All these elements tend to confirm that, in low-rate settings, the score distributions of JPEG AI pristine samples move above the 0 threshold. Hence, these images can be mistaken for deepfakes. On the contrary, for all detectors except [88]-B and [70], the FNR decreases for aggressive compression settings. This phenomenon seems to corroborate our intuition: JPEG AI artifacts might “overwrite” synthetic generation traces at very low BPP values. However, most detectors still mistake these artifacts as deepfake generation clues, thus reducing the FNR and ending up improving the classification performances of synthetic images.

As might be expected, when increasing the BPP, JPEG AI score distributions tend to align more closely with the original ones. Nonetheless, the BA can still be less than 0.7, and the FPR risks to be high even when the JPEG AI compression ratio gets lower (see the case in which BPP is equal to 1 for detectors [34]-A, [34]-B and [81]). Moreover, when the BPP increases, also a left-shift of the scores of synthetic samples can occur, thus resulting in a slight enhancement of FNR and reducing the detection performances (see, for instance, detectors [88]-A, [42], [32], [70] and [63]).

**JPEG AI image quality analysis.** Given the performance drop of all detectors when tested against JPEG AI images, we now investigate if this loss might be due to the poor visual quality of JPEG AI compressed images with respect to the original ones. To do this, we compute the Multi-scale SSIM (MS-SSIM) and the Visual Information Fidelity (VIF) for all the JPEG AI images in the datasets, comparing them to their JPEG AI-uncompressed versions. The JPEG AI committee proposes both metrics to evaluate the quality of JPEG AI implementations [1, 3]<sup>4</sup>.

Tab. 2 shows the average results. It is worth noticing

<sup>4</sup>Additional results available in Sec. 9.

Table 3. BA, FPR, and FNR evaluated at 0 threshold for the deepfake image detection case study before and after JPEG compression. AUC results available in the Supplementary Material Sec. 9.

	Original format			QF = 65			QF = 75			QF = 85			QF = 95		
	BA $\uparrow$	FPR $\downarrow$	FNR $\downarrow$	BA $\uparrow$	FPR $\downarrow$	FNR $\downarrow$	BA $\uparrow$	FPR $\downarrow$	FNR $\downarrow$	BA $\uparrow$	FPR $\downarrow$	FNR $\downarrow$	BA $\uparrow$	FPR $\downarrow$	FNR $\downarrow$
[88]-A	0.82	0.04	0.31	0.69	0.02	0.59	0.69	0.01	0.60	0.69	0.01	0.60	0.73	0.01	0.54
[88]-B	0.74	0.01	0.51	0.69	0.00	0.62	0.69	0.00	0.61	0.69	0.00	0.61	0.71	0.00	0.59
[42]	0.72	0.03	0.54	0.57	0.00	0.85	0.58	0.00	0.84	0.60	0.00	0.80	0.63	0.01	0.73
[32]	0.77	0.00	0.46	0.78	0.11	0.33	0.78	0.07	0.37	0.77	0.03	0.43	0.76	0.00	0.48
[70]	0.91	0.02	0.15	0.80	0.03	0.36	0.82	0.03	0.33	0.82	0.01	0.34	0.87	0.02	0.24
[34]-A	0.77	0.29	0.16	0.68	0.09	0.55	0.66	0.07	0.60	0.64	0.11	0.61	0.77	0.21	0.24
[34]-B	0.74	0.30	0.23	0.68	0.28	0.35	0.68	0.27	0.36	0.64	0.25	0.48	0.70	0.32	0.27
[81]	0.92	0.13	0.02	0.50	0.00	1.00	0.50	0.00	1.00	0.50	0.00	0.99	0.51	0.03	0.95
[63]	0.84	0.16	0.15	0.76	0.14	0.34	0.77	0.15	0.32	0.78	0.16	0.27	0.80	0.18	0.22

that all the considered BPP achieve high quality metrics. Extremely low BPP, as previously shown in Sec. 2, might carry a few low-pass filtering effects, but they do not introduce important losses in the visual quality of the images. This suggests that other artifacts than only low-pass frequency effects drive the detectors when classifying JPEG AI images as synthetic.

**Comparisons with standard JPEG.** In the forensic community, it is well-known that post-processing operations, especially image compression like standard JPEG, might alter the performance of detectors [32, 62, 88]. Thus, the results obtained using JPEG AI, as previously presented, could be considered somewhat predictable. Nonetheless, we argue that standard JPEG, while undermining the performance of detectors, behaves fundamentally differently from JPEG AI.

To investigate this, we compress our datasets using different Quality Factors (QFs), then compare the distribution of the scores before and after JPEG compression. Fig. 5 shows an example, i.e., the score distribution for the detector [34]-A from the LSUN dataset<sup>2</sup>. Notice that, differently from the JPEG AI case, the scores distribution of pristine JPEG-compressed images closely overlaps with those obtained from JPEG-uncompressed samples, meaning the absence of false alarms (both distributions are all centered below the 0). On the other hand, when compressing deepfake images, the scores distribution moves below the 0 as we increase the QF, meaning a significant increase in the number of false negatives.

To confirm this observation, Tab. 3 reports the average classification metrics for all datasets and detectors before (first left column) and after (starting from the second left column) JPEG varying the QF used in the compression. In this case, the BA has a general drop, which is more evident in the case of lower QFs. However, unlike the JPEG AI scenario, the FPR stays constant or even lowers, indicating that the scores distribution of pristine samples remains or moves even below the 0 threshold. On the other hand, JPEG compression, apart from detector [32], consistently affects the FNR, which is generally higher, especially for [88]-A, [42], [34]-A, [81] and [63]. This suggests that

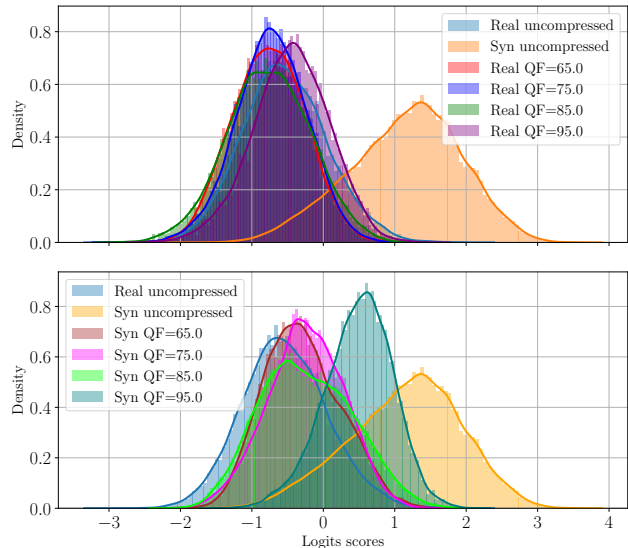


Figure 5. Scores distribution for [34]-A over LSUN *pristine* samples (top row) and their *synthetic* counterpart (bottom row) compressed with JPEG at different QF values.

JPEG compression shifts the scores distribution of deepfake images below the 0, effectively “canceling” out forensic artifacts that are crucial for deepfake detection. This behavior is diametrically opposed to that of JPEG AI, which essentially affects the detection of pristine content, increasing the number of false positives.

**Introducing JPEG AI into training.** Given that all the investigated detectors have not been trained with JPEG AI images, we conduct a last experiment by retraining the forensic detector recently proposed in [63] with JPEG AI samples. We consider the same data used in the training phase of this detector. However, we compress the 20% of training and validation samples with the BPP values considered in our previous analysis, equally distributed among the considered images. Then, we retrain this detector in two scenarios: (i) complete retraining over the same dataset used in [63], with 20% of its samples compressed with JPEG AI; (ii) a fine-tuning of the already trained detector by exploiting only JPEG AI samples. In both cases, we follow the

Table 4. Evaluation metrics for detector [63] before and after retraining or fine-tuning with 20% of JPEG AI samples. All metrics are computed with a 0 threshold.

	Original format			BPP = 0.12			BPP = 0.25			BPP = 0.5			BPP = 0.75			BPP = 1.0		
	BA $\uparrow$	FPR $\downarrow$	FNR $\downarrow$	BA $\uparrow$	FPR $\downarrow$	FNR $\downarrow$	BA $\uparrow$	FPR $\downarrow$	FNR $\downarrow$	BA $\uparrow$	FPR $\downarrow$	FNR $\downarrow$	BA $\uparrow$	FPR $\downarrow$	FNR $\downarrow$	BA $\uparrow$	FPR $\downarrow$	FNR $\downarrow$
Before	0.84	0.16	0.15	0.50	0.96	0.05	0.53	0.78	0.15	0.58	0.61	0.22	0.67	0.41	0.24	0.71	0.32	0.26
Retraining	0.83	0.15	0.19	0.61	0.65	0.14	0.69	0.41	0.21	0.74	0.25	0.27	0.76	0.19	0.29	0.77	0.16	0.30
Fine-tuning	0.81	0.07	0.31	0.58	0.63	0.21	0.64	0.43	0.28	0.73	0.24	0.31	0.76	0.17	0.32	0.76	0.14	0.33

original training procedure [63].

Tab. 4 depicts the achieved detection metrics over non-JPEG AI data (first left column) and over JPEG AI images (other columns) before and after retraining and fine-tuning. The detector is still capable of classifying original format samples, experiencing a slight performance loss in the retraining case and, as expected, a more significant drop when fine-tuning. Indeed, the fine-tuning setup includes only JPEG AI-compressed samples; thus, a subtle loss of generalization is expected.

As for what regards the BA and the FPR, we can notice a reduction of the JPEG AI counter-forensic effect since these metrics improve upon the initial results. Nonetheless, the BA is still below 0.7, and the FPR is above 0.4 for lower BPPs. Instead, the effects of retraining on the FNR are less visible: as observed before, though the FNR tends to reduce for low BPPs, this number gradually increases, achieving even higher values than those resulting when processing the original format images. These preliminary results show that a huge augmentation campaign should probably be considered to be completely robust to JPEG AI compression.

## 5.2. Image splicing localization

**Visual inspection.** As introduced in Sec. 4, we analyze three detectors, TruFor [43], MMFusion [85], and IFOSN [92]. We start by visually inspecting their output on a sample from the DSO-1 dataset. Figure 6 shows the output masks  $\tilde{M}$  for the original format as well as the masks obtained after compressing the input sample with JPEG AI at different BPPs for TruFor and MMFusion. We display the original spliced sample together with its compressed versions as well.

Even though the quality of the JPEG AI images is visually high, we can observe that the compression operation heavily degrades the output masks  $\tilde{M}$  in two different ways. First, for low BPP, the original manipulated area, while still largely identified, may present several false negatives, i.e., manipulated pixels that are incorrectly classified as pristine. Second, we can observe many false positives in the rest of the image, i.e., pristine pixels erroneously classified as manipulated at all BPP values. These two separate phenomena suggest that JPEG AI can contemporarily “hide” some manipulation traces while introducing artifacts mistaken for tampered with pixels.

**Quantitative analysis.** We compute the pixel-level local-

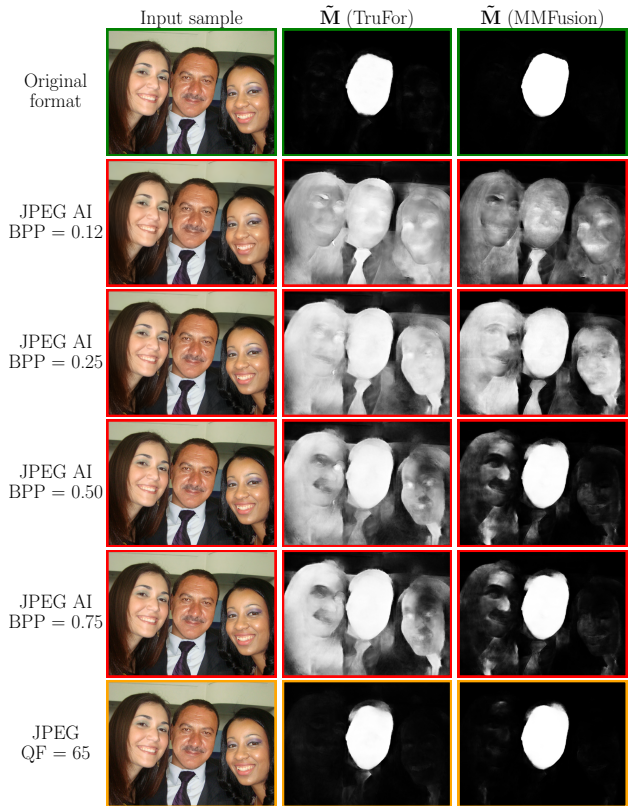


Figure 6. Output of TruFor [43] and MMFusion [85] for the same DSO-1 input under different JPEG AI compression settings, together with the JPEG QF = 65 setting. Other examples available in Sec. 10 of the supplementary material.

ization metrics illustrated in Sec. 4 to quantify this visual inspection and report their values in Tab. 5 (second and third right column). In particular, we calculate these metrics for all the datasets considered and then average their values.

As the reader can notice, performance drops sharply as the JPEG AI compression ratio increases for all detectors. For the compression at BPP = 0.12, we have a drop of more than 0.15 and 0.13 points in AUC and BA, respectively. Moreover, the F1 score sharply decreases by more than 0.28 points.

It is interesting to notice that, in high BPP settings, the F1 score may still show a drop of 0.10. Even if not visible to the naked eye, we conjecture that JPEG AI interpolation artifacts can impair the localization performance of the detectors considered. The IFOSN detector [92] is the least af-

Table 5. Image splicing localization results before and after JPEG AI and JPEG compressions for all detectors. Results are averaged per dataset, considering all datasets at disposal.

Metric	Orig. format	JPEG AI compressed (BPP)					JPEG compressed (QF)				
		0.12	0.25	0.5	0.75	1.0	65	75	85	95	
[43]	AUC	0.91	0.75	0.79	0.83	0.84	0.87	0.85	0.85	0.85	0.86
	BA	0.77	0.60	0.62	0.68	0.69	0.72	0.70	0.70	0.70	0.73
	F1	0.66	0.37	0.42	0.51	0.52	0.57	0.58	0.58	0.59	0.63
[85]	AUC	0.91	0.72	0.77	0.84	0.85	0.87	0.85	0.85	0.86	0.88
	BA	0.80	0.57	0.60	0.68	0.70	0.73	0.72	0.72	0.73	0.76
	F1	0.70	0.31	0.36	0.49	0.52	0.58	0.62	0.62	0.63	0.67
[92]	AUC	0.86	0.71	0.73	0.80	0.80	0.84	0.77	0.78	0.80	0.82
	BA	0.73	0.60	0.62	0.68	0.68	0.71	0.65	0.65	0.67	0.69
	F1	0.56	0.28	0.34	0.44	0.44	0.52	0.48	0.48	0.50	0.53

affected detector in case of high BPPs: we believe this might be due to its specific training process, developed for gaining robustness against social network compression.

**Comparison with standard JPEG.** The last row of Figure 6 shows the output masks  $\bar{M}$  obtained after compressing the input sample with JPEG at QF = 65 (i.e., the worst considered QF in our experiments) for TruFor [43] and MM-Fusion [85]. Notice the differences to JPEG AI: in the JPEG case, the localization performances are only slightly reduced, and the tampered with area is still well detectable.

We report in Tab. 5 (last column) the quantitative results for all detectors when tested against JPEG compression. It is worth noticing that JPEG impacts the detectors’ performance much less for all the QFs considered. In particular, even at the lowest QF, all metrics drop by a maximum of 0.09 points. We argue that, while JPEG is known for “hiding” tampering traces, JPEG AI has a considerably heavier effect due to the various upsampling artifacts introduced.

### 5.3. Double JPEG AI experiments.

A very common forensic scenario is that represented by double compression [20, 33, 96]. In this situation, the input samples might have undergone several compression stages before or after the manipulation. For instance, the manipulated area in a spliced sample might present traces of a compression operation performed before the splicing. Such traces can be extremely useful for understanding the overall image history and better localizing the tampered with pixels. Moreover, the double compression setup is also valuable for testing image detectors’ robustness, i.e., how good they are when analyzing images undergoing several compression stages.

In our work, we perform a preliminary analysis of the double compression scenario in the case of JPEG AI. To simplify the experimental setting, we consider two opposite setups: i) the original-format images have been JPEG AI-compressed with various BPP values and then compressed with the lowest BPP considered, i.e., BPP= 0.12; ii) the original-format images have been JPEG AI-compressed with various BPP values, and then compressed with the highest BPP considered, i.e., BPP= 2.0. For the sake of

space, we refer the reader to the supplementary material for an in-depth discussion. Our findings show that a strong second JPEG AI compression might cancel traces left by the previous compression step, similar to the behavior observed on standard double JPEG compression [20].

## 6. Discussion and conclusion

While far from being an exhaustive and complete analysis of the forensic implications of adopting JPEG AI, our results highlight how off-the-shelf forensic detectors need to be prepared to handle the artifacts of this upcoming standard. In both deepfake image detection and image splicing localization tasks, heavy compression leads to inaccurate classification of the investigated content, requiring practitioners to consider JPEG AI images in their work.

As the boundaries between synthetic and authentic media continue to thin [68], these findings open up new avenues for multimedia forensic researchers on both a general and technical level. On a more general level, the broad adoption of NNs in processing media of any kind requires practitioners to reflect on the very nature of the task of deepfake media detection. In a scenario where all media are “deepfakes”, meaning that they went through some NN processing, multimedia forensics will have to go deeper in its analysis. For instance, it will be required to understand if that particular processing was meant for harmful purposes, e.g., to create a deepfake for fake news propaganda, or for innocuous tasks, e.g., for image compression or quality enhancement. Recent works on avatar fingerprints [74] go in this direction. In such a scenario, there is also a growing demand for active mechanisms that guarantee the media’s provenance, integrity, and reliability. The Content Authenticity Initiative by Adobe [5], as well as the JPEG Trust standard [4], are being developed and adopted in this vein.

On a more technical level, and for the time being, multimedia forensic researchers must develop techniques robust to neural compression artifacts. Robustness to post-processing operations [21, 25, 62, 63, 88, 89] and adversarial attacks [27, 48, 77] are well-known and studied topics in multimedia forensics. However, the nature of neural image compression calls for detectors that distinguish between “genuine” neural artifacts and those left by “malicious” generation techniques. Correct re-training of data-driven detectors, as shown in Sec. 5 or as proposed in [63], are all valid options to further investigate in conjunction with the more general reformulation of the deepfake detection task mentioned above.

In conclusion, the diffusion of JPEG AI fits in a rapidly changing landscape, requiring multimedia forensics to develop more robust instruments and collaborate with social and legal entities to fight against disinformation and re-introduce trust in all media types.

## References

- [1] Jpeg call for evidence on learning-based image coding solutions, 2020. © 2020. All rights reserved. 2, 4, 5, 3
- [2] Dall-e mini, 2021. 2
- [3] White paper on jpeg ai scope and framework. <https://ds.jpeg.org/whitepapers/jpeg-ai-whitepaper.pdf>, 2021. Accessed: 2024-11-11. 1, 5
- [4] Jpeg trust: an international standard for establishing trust in digital media. <https://ds.jpeg.org/whitepapers/jpeg-trust-whitepaper.pdf>, 2024. Accessed: 2024-11-11. 8
- [5] Content authenticity initiative. <https://contentauthenticity.org/>, 2024. Accessed: 2024-11-11. 8
- [6] Dall-e 2. <https://openai.com/index/dall-e-2/>, 2024. Accessed: 2024-11-13. 2
- [7] Dall-e 3. <https://openai.com/index/dall-e-3/>, 2024. Accessed: 2024-11-13. 2
- [8] Adobe firefly. <https://www.adobe.com/it/products/firefly.html>, 2024. Accessed: 2024-11-13. 2
- [9] Jpeg ai reaches draft international standard stage, 2024. © 2024. All rights reserved. 2
- [10] Jpeg ai reference software, 2024. © 2024. All rights reserved. 2, 4, 3
- [11] Midjourney. <https://www.midjourney.com/home>, 2024. Accessed: 2024-11-13. 2
- [12] Stable diffusion v1-3. <https://huggingface.co/CompVis/stable-diffusion-v1-3>, 2024. Accessed: 2024-11-13. 2
- [13] Stable diffusion v1-4. <https://huggingface.co/CompVis/stable-diffusion-v1-4>, 2024. Accessed: 2024-11-13. 2
- [14] Stable diffusion 2.1. <https://huggingface.co/spaces/stabilityai/stable-diffusion>, 2024. Accessed: 2024-11-13. 2
- [15] Stable diffusion xl. <https://huggingface.co/stabilityai/stable-diffusion-xl-base-0.9>, 2024. Accessed: 2024-11-13. 2
- [16] Jpeg ai becomes an international standard, 2025. © 2025. All rights reserved. 1, 2
- [17] Joao Ascenso, Elena Alshina, and Touradj Ebrahimi. The JPEG AI standard: Providing efficient human and machine visual data consumption. *IEEE Multimedia*, 30(1):100–111, 2023. 1, 2
- [18] Johannes Ballé, Valero Laparra, and Eero P. Simoncelli. End-to-end optimized image compression. In *International Conference on Learning Representations*, 2017. 1
- [19] Johannes Ballé, David Minnen, Saurabh Singh, Sung Jin Hwang, and Nick Johnston. Variational image compression with a scale hyperprior. In *International Conference on Learning Representations*, 2018. 1
- [20] Mauro Barni, Luca Bondi, Nicolò Bonettini, Paolo Bestagini, Andrea Costanzo, Marco Maggini, Benedetta Tondi, and Stefano Tubaro. Aligned and non-aligned double jpeg detection using convolutional neural networks. *Journal of Visual Communication and Image Representation*, 49: 153–163, 2017. 8
- [21] Mauro Barni, Matthew C. Stamm, and Benedetta Tondi. Adversarial multimedia forensics: Overview and challenges ahead. In *2018 26th European Signal Processing Conference (EUSIPCO)*, 2018. 8
- [22] Sandra Bergmann, Denise Moussa, Fabian Brand, André Kaup, and Christian Riess. Frequency-domain analysis of traces for the detection of ai-based compression. In *2023 11th International Workshop on Biometrics and Forensics (IWFBF)*, 2023. 1, 2
- [23] Sandra Bergmann, Denise Moussa, Fabian Brand, André Kaup, and Christian Riess. Forensic analysis of ai-compression traces in spatial and frequency domain. *Pattern Recognition Letters*, 180:41–47, 2024. 1, 2
- [24] Alexandre Berthet and Jean-Luc Dugelay. Ai-based compression: A new unintended counter attack on jpeg-related image forensic detectors? In *2022 IEEE International Conference on Image Processing (ICIP)*, 2022. 2
- [25] Luca Bondi, Edoardo Daniele Cannas, Paolo Bestagini, and Stefano Tubaro. Training strategies and data augmentations in cnn-based deepfake video detection. 2020. 8
- [26] Andrew Brock, Jeff Donahue, and Karen Simonyan. Large scale GAN training for high fidelity natural image synthesis. In *International Conference on Learning Representations*, 2019. 2
- [27] Nicholas Carlini and Hany Farid. Evading deepfake-image detectors with white- and black-box attacks. In *2020 IEEE/CVF Conference on Computer Vision and Pattern Recognition Workshops (CVPRW)*, pages 2804–2813, 2020. 8
- [28] Tiago Carvalho, Fábio A. Faria, Hélio Pedrini, Ricardo da S. Torres, and Anderson Rocha. Illuminant-based transformed spaces for image forensics. *IEEE Transactions on Information Forensics and Security*, 2016. 4
- [29] Yunjey Choi, Minje Choi, Munyoung Kim, Jung-Woo Ha, Sunghun Kim, and Jaegul Choo. Stargan: Unified generative adversarial networks for multi-domain image-to-image translation. In *Proceedings of the IEEE Conference on Computer Vision and Pattern Recognition*, 2018. 2
- [30] Yochai Choi, Mostafa El-Khamy, and Jungwon Lee. Variable rate deep image compression with a conditional autoencoder. In *2019 IEEE/CVF International Conference on Computer Vision (ICCV)*, pages 3146–3154, 2019. 1
- [31] Riccardo Corvi, Davide Cozzolino, Giovanni Poggi, Koki Nagano, and Luisa Verdoliva. Intriguing properties of synthetic images: From generative adversarial networks to diffusion models. In *Proceedings of the IEEE/CVF Conference on Computer Vision and Pattern Recognition (CVPR) Workshops*, pages 973–982, 2023. 1
- [32] Riccardo Corvi, Davide Cozzolino, Giada Zingarini, Giovanni Poggi, Koki Nagano, and Luisa Verdoliva. On the detection of synthetic images generated by diffusion models. In *IEEE International Conference on Acoustics, Speech and Signal Processing (ICASSP)*, pages 1–5, 2023. 2, 3, 5, 6, 1, 13

- [33] Davide Cozzolino, Giovanni Poggi, and Luisa Verdoliva. Splicebuster: A new blind image splicing detector. In *2015 IEEE International Workshop on Information Forensics and Security (WIFS)*, pages 1–6. IEEE, 2015. 8
- [34] Davide Cozzolino, Giovanni Poggi, Riccardo Corvi, Matthias Nießner, and Luisa Verdoliva. Raising the Bar of AI-generated Image Detection with CLIP. In *IEEE/CVF Conference on Computer Vision and Pattern Recognition Workshops (CVPRW)*, 2024. 3, 5, 6, 1, 2, 7, 8, 13
- [35] Duc-Tien Dang-Nguyen, Cecilia Pasquini, Valentina Conotter, and Giulia Boato. Raise – a raw images dataset for digital image forensics. In *Proceedings of the ACM Multimedia Systems Conference*, 2015. 4
- [36] Tiago José de Carvalho, Christian Riess, Elli Angelopoulou, Hélio Pedrini, and Anderson de Rezende Rocha. Exposing digital image forgeries by illumination color classification. *IEEE Transactions on Information Forensics and Security*, 2013. 4
- [37] Jia Deng, Wei Dong, Richard Socher, Li-Jia Li, Kai Li, and Li Fei-Fei. Imagenet: A large-scale hierarchical image database. In *2009 IEEE Conference on Computer Vision and Pattern Recognition*, pages 248–255, 2009. 4
- [38] Prafulla Dhariwal and Alex Nichol. Diffusion models beat gans on image synthesis. In *Proceedings of the 35th International Conference on Neural Information Processing Systems*, 2021. 2
- [39] Jing Dong, Wei Wang, and Tieniu Tan. Casia image tampering detection evaluation database. In *2013 IEEE China Summit and International Conference on Signal and Information Processing*, pages 422–426, 2013. 4
- [40] Ricard Durall, Margret Keuper, and Janis Keuper. Watch your Up-Convolution: CNN Based Generative Deep Neural Networks are Failing to Reproduce Spectral Distributions. In *IEEE Conference on Computer Vision and Pattern Recognition (CVPR)*, 2020. 1
- [41] Patrick Esser, Robin Rombach, and Bjorn Ommer. Taming transformers for high-resolution image synthesis. In *Proceedings of the IEEE/CVF Conference on Computer Vision and Pattern Recognition (CVPR)*, pages 12873–12883, 2021. 2
- [42] Diego Gagnaniello, Davide Cozzolino, Francesco Marra, Giovanni Poggi, and Luisa Verdoliva. Are GAN generated images easy to detect? a critical analysis of the state-of-the-art. In *IEEE International Conference on Multimedia and Expo (ICME)*, pages 1–6. IEEE, 2021. 1, 3, 5, 6, 2, 13, 17
- [43] Fabrizio Guillaro, Davide Cozzolino, Avneesh Sud, Nicholas Dufour, and Luisa Verdoliva. Trufor: Leveraging all-round clues for trustworthy image forgery detection and localization. In *Proceedings of the IEEE/CVF Conference on Computer Vision and Pattern Recognition (CVPR)*, pages 20606–20615, 2023. 4, 7, 8
- [44] K. He, X. Zhang, S. Ren, and J. Sun. Deep residual learning for image recognition. In *2016 IEEE Conference on Computer Vision and Pattern Recognition (CVPR)*, pages 770–778, 2016. 1
- [45] Nora Hofer and Rainer Böhme. A taxonomy of miscompressions: Preparing image forensics for neural compression, 2024. 1, 2
- [46] Emiel Hoogeboom, Eirikur Agustsson, Fabian Mentzer, Luca Versari, George Toderici, and Lucas Theis. High-fidelity image compression with score-based generative models. *arXiv preprint arXiv:2305.18231*, 2023. 1
- [47] Y.-F. Hsu and S.-F. Chang. Detecting image splicing using geometry invariants and camera characteristics consistency. In *International Conference on Multimedia and Expo*, 2006. 4
- [48] Shehzeen Hussain, Paarth Neekhara, Malhar Jere, Farinaz Koushanfar, and Julian McAuley. Adversarial deepfakes: Evaluating vulnerability of deepfake detectors to adversarial examples. In *Proceedings of the IEEE/CVF Winter Conference on Applications of Computer Vision (WACV)*, pages 3348–3357, 2021. 8
- [49] ISO/IEC JTC 1/SC 29/WG 1. Coding of still pictures. Technical Report N83058, International Organization for Standardization and International Electrotechnical Commission, 2019. JPEG AI investigations start. 1
- [50] ISO/IEC JTC 1/SC 29/WG 1. Jpeg ai overview slides. Technical Report N100658, International Organization for Standardization and International Electrotechnical Commission, 2023. JPEG AI overview. 2, 1
- [51] ISO/IEC JTC 1/SC 29/WG 1. Jpeg ai use cases and requirements. Technical Report N100724, International Organization for Standardization and International Electrotechnical Commission, 2023. JPEG AI use case and requirements. 1
- [52] Tero Karras, Timo Aila, Samuli Laine, and Jaakko Lehtinen. Progressive growing of gans for improved quality, stability, and variation. In *Proceedings of the International Conference on Learning Representations*, 2018. 1, 2
- [53] Tero Karras, Samuli Laine, and Timo Aila. A style-based generator architecture for generative adversarial networks. In *Proceedings of the IEEE/CVF Conference on Computer Vision and Pattern Recognition (CVPR)*, 2019. 2
- [54] Tero Karras, Samuli Laine, and Timo Aila. A style-based generator architecture for generative adversarial networks. In *2019 IEEE/CVF Conference on Computer Vision and Pattern Recognition (CVPR)*, pages 4396–4405, 2019. 2, 4
- [55] Tero Karras, Samuli Laine, Miika Aittala, Janne Hellsten, Jaakko Lehtinen, and Timo Aila. Analyzing and improving the image quality of StyleGAN. In *Proceedings of the IEEE/CVF Conference on Computer Vision and Pattern Recognition (CVPR)*, 2020. 2
- [56] Alexander Kolesnikov, Alexey Dosovitskiy, Dirk Weissenborn, Georg Heigold, Jakob Uszkoreit, Lucas Beyer, Matthias Minderer, Mostafa Dehghani, Neil Houlsby, Sylvain Gelly, Thomas Unterthiner, and Xiaohua Zhai. An image is worth 16x16 words: Transformers for image recognition at scale. 2021. 1
- [57] Valero Laparra, Johannes Ballé, Anthony Bernardino, and Eero P. Simoncelli. Perceptual image quality assessment using a normalized laplacian pyramid. In *S&T Symposium on Electronic Imaging: Conf. on Human Vision and Electronic Imaging*, 2016. 2
- [58] Zhi Li, A. Aaron, I. Katsavounidis, A. Moorthy, and M. Manohara. Toward a practical perceptual video quality metric. <https://netflixtechblog.com/toward->

a-practical-perceptual-video-quality-metric-653f208b9652. Accessed: 2024-11-12. 3

- [59] Kelsey Lieberman, James Diffenderfer, Charles Godfrey, and Bhavya Kailkhura. Neural image compression: Generalization, robustness, and spectral biases. In *Advances in Neural Information Processing Systems*, 2023. 1
- [60] Tsung-Yi Lin, Michael Maire, Serge J. Belongie, James Hays, Pietro Perona, Deva Ramanan, Piotr Dollár, and C. Lawrence Zitnick. Microsoft coco: Common objects in context. In *European Conference on Computer Vision*, 2014. 4
- [61] Ziwei Liu, Ping Luo, Xiaogang Wang, and Xiaoou Tang. Deep learning face attributes in the wild. In *Proceedings of International Conference on Computer Vision (ICCV)*, 2015. 4
- [62] Sara Mandelli, Nicolo Bonettini, Paolo Bestagini, and Stefano Tubaro. Training cnns in presence of jpeg compression: Multimedia forensics vs computer vision. In *2020 IEEE International Workshop on Information Forensics and Security (WIFS)*, pages 1–6. IEEE, 2020. 6, 8
- [63] Sara Mandelli, Paolo Bestagini, and Stefano Tubaro. When synthetic traces hide real content: Analysis of stable diffusion image laundering. In *Proceedings of the IEEE International Workshop on Information Forensics and Security (WIFS)*, 2024. 1, 2, 3, 5, 6, 7, 8, 13
- [64] Fabian Mentzer, Eirikur Agustsson, Michael Tschannen, Radu Timofte, and Luc Van Gool. High-fidelity generative image compression. *arXiv preprint arXiv:2006.09965*, 2020. 1
- [65] David Minnen and Saurabh Singh. Channel-wise autoregressive entropy models for learned image compression. In *IEEE International Conference on Acoustics, Speech, and Signal Processing (ICASSP)*. IEEE, 2020.
- [66] David Minnen, Johannes Ballé, and George D. Toderici. Joint autoregressive and hierarchical priors for learned image compression. *Advances in Neural Information Processing Systems*, 31, 2018. 1
- [67] Deepak Mishra, Sharad K. Singh, and Ranjan K. Singh. Deep architectures for image compression: A critical review. *Signal Processing*, 191:108346, 2022. 2
- [68] Daniel Moreira, Sébastien Marcel, and Anderson Rocha. Synthetic realities and artificial intelligence-generated contents. *IEEE Security & Privacy*, 22(3):7–10, 2024. 8
- [69] Alexander Quinn Nichol, Prafulla Dhariwal, Aditya Ramesh, Pranav Shyam, Pamela Mishkin, Bob McGrew, Ilya Sutskever, and Mark Chen. GLIDE: Towards photorealistic image generation and editing with text-guided diffusion models. In *Proceedings of the 39th International Conference on Machine Learning*, 2022. 2
- [70] Utkarsh Ojha, Yuheng Li, and Yong Jae Lee. Towards universal fake image detectors that generalize across generative models. In *Proceedings of the IEEE/CVF Conference on Computer Vision and Pattern Recognition (CVPR)*, pages 24480–24489, 2023. 3, 5, 6, 1, 2, 9, 10, 13
- [71] Britt Paris and Joan Donovan. Deepfakes and cheap fakes. *Data & Society*, 2019. 3
- [72] Taesung Park, Ming-Yu Liu, Ting-Chun Wang, and Jun-Yan Zhu. Gaugan: semantic image synthesis with spatially adaptive normalization. *ACM SIGGRAPH 2019 Real-Time Live!*, 2019. 2
- [73] A. Piva. An overview on image forensics. *ISRN Signal Processing*, 2013. 3
- [74] Ekta Prashnani, Koki Nagano, Shalini De Mello, David Luebke, and Orazio Gallo. Avatar fingerprinting for authorized use of synthetic talking-head videos. *arXiv preprint arXiv:2305.03713*, 2023. 8
- [75] Aditya Ramesh, Mikhail Pavlov, Gabriel Goh, Scott Gray, Chelsea Voss, Alec Radford, Mark Chen, and Ilya Sutskever. Zero-shot text-to-image generation. In *Proceedings of the 38th International Conference on Machine Learning*, 2021. 2
- [76] Robin Rombach, Andreas Blattmann, Dominik Lorenz, Patrick Esser, and Björn Ommer. High-resolution image synthesis with latent diffusion models. In *Proceedings of the IEEE/CVF Conference on Computer Vision and Pattern Recognition (CVPR)*, 2022. 1, 2
- [77] Vincenzo De Rosa, Fabrizio Guillaro, Giovanni Poggi, Davide Cozzolino, and Luisa Verdoliva. Exploring the adversarial robustness of clip for ai-generated image detection. In *Proceedings of the IEEE International Workshop on Information Forensics and Security (WIFS)*, 2024. 8
- [78] Christoph Schuhmann, Richard Vencu, Romain Beaumont, Robert Kaczmarczyk, Clayton Mullis, Aarush Katta, Theo Coombes, Jenia Jitsev, and Aran Komatsuzaki. Laion-400m: Open dataset of clip-filtered 400 million image-text pairs, 2021. 4
- [79] H.R. Sheikh and Alan C. Bovik. Image information and visual quality. In *IEEE International Conference on Acoustics, Speech, and Signal Processing*, 2004. 2
- [80] M. C. Stamm, Min Wu, and K. J. R. Liu. Information forensics: An overview of the first decade. *IEEE Access*, 1:167–200, 2013. 1
- [81] Chuangchuan Tan, Yao Zhao, Shikui Wei, Guanghua Gu, Ping Liu, and Yunchao Wei. Rethinking the up-sampling operations in cnn-based generative network for generalizable deepfake detection. In *Proceedings of the IEEE/CVF Conference on Computer Vision and Pattern Recognition (CVPR)*, pages 28130–28139, 2024. 1, 3, 5, 6, 2, 11, 12, 14
- [82] Mingxing Tan and Quoc V. Le. Efficientnet: Rethinking model scaling for convolutional neural networks. In *International Conference on Machine Learning (ICML) 2019*, pages 6105–6114. PMLR, 2019. 2
- [83] Lucas Theis, Wenzhe Shi, Andrew Cunningham, and Ferenc Huszár. Lossy image compression with compressive autoencoders. 2017. 1
- [84] George D. Toderici, Damien Vincent, Nick Johnston, Sung Jin Hwang, David Minnen, Joel Shor, and Michele Covell. Full resolution image compression with recurrent neural networks. *IEEE Conference on Computer Vision and Pattern Recognition*, pages 5306–5314, 2017. 1
- [85] Konstantinos Triaridis and Vasileios Mezaris. Exploring multi-modal fusion for image manipulation detection and localization. In *Proc. 30th Int. Conf. on MultiMedia Modeling (MMM 2024)*, 2024. 4, 7, 8

- [86] Daria Tserch, Mark Mirgaleev, Ivan Molodetskikh, Roman Kazantsev, and Dmitriy Vatolin. Jpeg ai image compression visual artifacts: Detection methods and dataset, 2024. [1](#), [2](#)
- [87] Luisa Verdoliva. Media forensics and deepfakes: an overview. *IEEE journal of selected topics in signal processing*, 14(5):910–932, 2020. [3](#)
- [88] Sheng-Yu Wang, Oliver Wang, Richard Zhang, Andrew Owens, and Alexei A Efros. CNN-generated images are surprisingly easy to spot... for now. In *IEEE/CVF Conference on Computer Vision and Pattern Recognition*, pages 8695–8704, 2020. [1](#), [3](#), [5](#), [6](#), [8](#), [2](#), [4](#), [10](#), [12](#)
- [89] Tianyi Wang, Xin Liao, Kam Pui Chow, Xiaodong Lin, and Yinglong Wang. Deepfake detection: A comprehensive survey from the reliability perspective. *ACM Comput. Surv.*, 2024. [8](#)
- [90] Zhou Wang, Eero P. Simoncelli, and Alan C. Bovik. Multi-scale structural similarity for image quality assessment. In *37th IEEE Asilomar Conference on Signals, Systems and Computers*, 2003. [2](#)
- [91] Bihan Wen, Ye Zhu, Ramanathan Subramanian, Tian-Tsong Ng, Xuanjing Shen, and Stefan Winkler. Coverage – a novel database for copy-move forgery detection. In *IEEE International Conference on Image processing (ICIP)*, pages 161–165, 2016. [4](#)
- [92] Haiwei Wu, Jiantao Zhou, Jinyu Tian, Jun Liu, and Yu Qiao. Robust image forgery detection against transmission over online social networks. *IEEE Transactions on Information Forensics and Security*, 17:443–456, 2022. [4](#), [7](#), [8](#)
- [93] Feng Yang, Lucas Herranz, Yong Cheng, and M. G. Mozerov. Slimmable compressive autoencoders for practical neural image compression. In *Proceedings of the IEEE/CVF Conference on Computer Vision and Pattern Recognition (CVPR)*, pages 4998–5007, 2021. [1](#)
- [94] Ruihan Yang and Stephan Mandt. Lossy image compression with conditional diffusion models. In *Advances in Neural Information Processing Systems*, 2023. [1](#)
- [95] Fisher Yu, Ari Seff, Yinda Zhang, Shuran Song, Thomas Funkhouser, and Jianxiong Xiao. LSUN: Construction of a large-scale image dataset using deep learning with humans in the loop. Technical Report 1506.03365, arXiv preprint, 2015. [2](#), [4](#)
- [96] Markos Zampoglou, Symeon Papadopoulos, and Yiannis Kompatsiaris. Large-scale evaluation of splicing localization algorithms for web images. *Multimedia Tools and Applications*, 76(4):4801–4834, 2017. [8](#)
- [97] Lin Zhang, Lei Zhang, Xuanqin Mou, and David Zhang. Fsim: a feature similarity index for image quality assessment. *IEEE Transactions on Image Processing*, 20(8):2378–2386, 2011. [2](#)
- [98] Xiaoheng Zhu, Jingwen Song, Liyuan Gao, Fanglong Zheng, and Heng Tao Shen. Unified multivariate gaussian mixture for efficient neural image compression. In *Proceedings of the IEEE/CVF Conference on Computer Vision and Pattern Recognition (CVPR)*, pages 17612–17621, 2022. [1](#)

# Is JPEG AI going to change image forensics?

## Supplementary Material

### 7. Neural image compression and JPEG AI specification

**Neural image compression basics.** In Neural Image Compression (NIC), an input image is transformed into a compact file or bitstream for storage or transmission, which is later used to reconstruct the original image. The basic approach involves mapping an image vector  $\mathbf{I}$  to a latent representation  $\mathbf{y}$  using a convolutional autoencoder. This latent representation is then quantized to  $\hat{\mathbf{y}}$  and compressed into a bitstream using an entropy coding method such as arithmetic coding. During reconstruction, the received bits are decoded via reverse entropy coding, and the resulting  $\hat{\mathbf{y}}$  is fed into a CNN decoder to produce the reconstructed image  $\hat{\mathbf{I}}$ . These models can be trained end-to-end with the help of differentiable proxies for entropy coding.

As pointed out in Sec. 2, many techniques exist to perform such operations. In 2017, Theis et al. [83] and Ballé et al. [18] introduced the first deep-learning approaches for image compression. [83] proposed compressive autoencoders that learn end-to-end optimized lossy image compression, aiming to outperform traditional codecs, especially at lower bitrates. [18] presented the first pipeline that jointly optimizes all components of the compression pipeline, achieving superior rate-distortion performance compared to traditional codecs. Building upon their previous work, in [19], Ballé et al. incorporate a scale hyperprior to model the entropy of the latent representations more accurately, leading to improved compression efficiency. Minnen et al. [66] combine autoregressive models with hierarchical priors to better capture spatial dependencies in images, enhancing the performance of learned image compression systems. Choi et al. [30] present a conditional autoencoder that enables variable-rate image compression within a single model, adjusting compression rates on the fly without retraining. In 2021, Yang et al. [93] proposed slimmable autoencoders that adjust their network width to accommodate different compression rates, making neural compression more adaptable and efficient. Zhu et al. [98] in 2022 presented a unified entropy model using multivariate Gaussian mixtures to better model the distribution of latent representations, improving compression efficiency.

**JPEG AI scheme specification.** The astonishing results from the literature pushed in 2019 the JPEG Standardization Committee to launch the first image coding specifications based on end-to-end learning [49], namely the JPEG AI initiative. At its core, JPEG AI follows a similar structure to standard neural image compression algorithms. In particular, we refer the reader to Fig. 2 [50] for the overall

JPEG AI standard scheme specification. The encoder consists of a NN-based analysis transform that computes the latent information  $\mathbf{y}$  of the input image  $\mathbf{I}$ . Next,  $\mathbf{y}$  is processed by a latent domain prediction module, generating a latent residual  $\hat{\mathbf{f}}$ , and by a hyperprior encoder, producing a hyperprior  $\hat{\mathbf{z}}$ , as proposed in the foundational work by Ballé et al. [19]. For entropy decoding, a latent prediction network retrieves  $\hat{\mathbf{y}}$ , which is finally input into the synthesis transform at the decoder for reconstructing the image  $\hat{\mathbf{I}}$ .

As explained in Sec. 2, JPEG AI enforces strict compliance requirements on manufacturers as a standardized format, limiting the customization options within the compression pipeline. Although certain architectural modifications are permitted (indicated by the red modules of Fig. 2), such as adjustments to the analysis transform, to the hyperprior encoder network, or retraining for specific content types to improve performance, these changes are restricted. The modified latent space must still function within the official JPEG AI framework to ensure compatibility [50].

### 8. Experimental setup additional details

**Experiments reproducibility.** All code and additional figures and tables for all detectors is available at the following URL <https://github.com/polimi-ispl/jpeg-ai-antifor>.

**Deepfake image detectors.** We provide some more information regarding the forensic detectors presented in Sec. 4:

- [88]: a ResNet-50 [44], pre-trained on the Imagenet dataset and then finetuned on a dataset of real and deepfake images generated through the ProGAN [52] architecture. This detector is available in two variants, i.e., [88]-A, trained with an augmentation of Gaussian blurring and JPEG compression applied to each image with a probability of 10%, and [88]-B, trained with the same augmentation pipeline but applied with a probability of 50%;
- [42]: another ResNet-50 trained with the same setup of [88], however avoiding down-sampling of the features extracted in the first layer of the network;
- [32]: same solution as [42], but in this case, the authors train the network on a dataset of Latent Diffusion [76] deepfake samples;
- [70]: a frozen Vision Transformer (ViT) [56] pre-trained on the CLIP task, to which a final classification layer is finetuned with same dataset of [88];
- [34]: a similar approach to [70], where the authors substitute the final classification layer with a Support Vector Machine (SVM). The SVM is finetuned with only 1000

real samples from the COCO datasets and 1000 deepfakes generated with Latent Diffusion. In this case, too, we have two variants of the detector, i.e., [34]-A, trained without augmentation, and [34]-B, trained with compression and resize as data augmentation;

- [63]: an EfficientNet-B4 [82] performing a patch-based analysis of the image and aggregating multiple scores to decide the “fakeness” of the sample. This detector is trained exclusively on datasets of human faces, with deepfake samples coming from various generators, including GANs, transformers, and diffusion models;
- [81]: a method focusing on detecting deepfakes by analyzing structural artifacts introduced during the up-sampling operations in generative networks like GANs and diffusion models, namely Neighboring Pixel Relationships (NPR). These artifacts create local interdependencies among neighboring pixels in synthetic images. NPR captures and characterizes these relationships to identify forgeries effectively.

**Deepfake datasets.** To test the performances of every detector in normal conditions, we include for every pristine test set a deepfake “counterpart”. These images have been selected by the original authors of the detectors to depict content similar to that of the pristine ones but are generated using different deepfake image generation techniques. In total, we considered 20 different generation techniques ranging from GANs to diffusion models, namely Guided Diffusion [38], Latent Diffusion [76], Taming Transformers [41], DALL-E [75] in various versions (i.e., mini [2], 2 [6], and 3 [7]), GLIDE [69], Stable Diffusion [76] in various versions (i.e., 1.3 [12], 1.4 [13], XL [15], and 2 [14]), Adobe Firefly [8], MidJourney v5 [11], BigGAN [26], GauGAN [72], StyleGAN [53], StyleGAN2 [55], ProGAN [52], and StarGAN [29]. Tab. 6 report their relationships with the different pristine datasets used in our evaluation.

## 9. Deepfake image detection additional results

**Preliminary analysis on synthetic detection.** Tab. 7 reports the results for the simple case of synthetic image detection *without* JPEG AI image compression of the test samples. We report the complete numbers for all detectors on all datasets.

We tested each detector only on the datasets on which the original authors first proposed the method. [63] represents the only exception since the authors reported good generalization capabilities on various semantic content despite training their solution only on human faces. As the reader can quickly inspect, all detectors achieve acceptable performance, with only two cases below the 0.75 threshold for the AUC, i.e., [34]-B on LAION and [63] on COCO.

**JPEG AI quality analysis.** Tab. 8 reports a complete quality analysis of the pristine JPEG AI compressed samples. To achieve this, we computed the following metrics:

Table 6. Deepfake image generation techniques used in our experiments and their relationships with pristine datasets’ content.

	CelebA	COCO	FFHQ	Imagenet	LAION	LSUN	RAISE
BigGAN [26]				✓			
GauGAN [72]		✓					
ProGAN [52]						✓	
StarGAN [29]	✓						
StyleGAN [53]						✓	
StyleGAN2 [55]			✓			✓	
GLIDE [69]		✓			✓		✓
Guided Diffusion [38]				✓	✓	✓	
Latent Diffusion [76]		✓	✓	✓		✓	
Taming Transformers [41]			✓	✓			
DALL-E [2, 6, 7, 75]		✓			✓		✓
Stable Diffusion [12–15, 76]		✓					✓
Adobe Firefly [8]							✓
MidJourney v5 [11]							✓

Table 7. AUC results of the various detectors on all datasets considered for the real VS synthetic image detection task. Results below the 0.75 threshold are reported in red. Entries signed with a – indicate that the detector has not been tested on that particular dataset.

Detector	Dataset						
	LSUN	Imagenet	COCO	CelebA	FFHQ	LAION	RAISE
[88]-A	0.99	0.88	0.92	0.98	–	–	–
[88]-B	0.98	0.90	0.98	0.95	–	–	–
[42]	–	0.89	0.96	–	0.93	–	–
[32]	–	0.87	0.96	–	0.89	–	–
[70]	0.98	0.99	1.00	0.99	–	0.96	–
[34]-A	0.95	0.97	0.97	–	0.96	0.96	0.80
[34]-B	0.79	0.83	0.89	–	0.88	<b>0.74</b>	0.86
[81]	0.94	0.91	1.00	1.00	–	0.99	–
[63]	0.86	0.87	<b>0.71</b>	1.00	1.00	0.98	0.83

- Feature Similarity (FSIM) [97]: a metric based on phase congruency and gradient magnitude to assess quality. The value range for FS is between 0 and 1, with 1 indicating the highest quality;
- Multi-Scale SIMilarity index (MS-SSIM) [90]: evaluates image quality by comparing details across resolutions. Typical values range between 0 and 1, with 1 indicating the highest quality;
- Normalized Laplacian Pyramid (NLP) [57]: based on local luminance and contrast, it uses a Laplacian pyramid decomposition. We normalize the scores in a 0 – 1 range, with 1 indicating higher quality;
- Visual Information Fidelity (VIF) [79]: measures the loss

of perceived information using natural scene statistics. Values range from 0 to infinity, with higher scores indicating better quality;

- Video Multimethod Assessment Fusion (VMAF) [58]: developed by Netflix, it assesses quality by fusing scores from multiple algorithms. Scores range from 0 to 100, with high values indicating better quality.

All these metrics have been suggested in the JPEG AI Call For Evidence [1], and we computed them using the official JPEG AI Reference Software [10]. The samples present an overall high perceptual quality as the reader can quickly inspect, even at low BPP values.

**Scores distributions.** Fig. 7 to Fig. 13 report the scores distribution of the detectors [42], [34]-A, [70], and [81] while varying the JPEG AI compression ratio or the JPEG quality factor of the compressed images. We report one plot for each dataset on which we tested the detectors. Results are in line with the ones reported in Fig. 4 and Fig. 5 of the main paper: while increasing the JPEG AI compression ratio creates a “shift” of the scores distribution towards the right, i.e., towards “deepfake”-like scores above the 0 threshold, standard JPEG moves the distribution towards the left, i.e., towards “pristine”-like scores below the 0 threshold. Such results are particularly relevant for the [81] detector. This tool looks for NPR, i.e., the local interdependence between image pixels caused by up-sampling operators. Such a trace seems particularly sensitive to JPEG compression. Indeed, we can see in Fig. 12d and Fig. 12f how even the score distribution for pristine samples is moved below the distribution of pristine uncompressed images. However, this result should not surprise us, as it is well known in the forensic community that JPEG compression could conceal traces relative to the image history [73]. We refer the reader to the code repository to visualize more distribution score plots.

**Complete analysis of JPEG AI compression ratio.** Tab. 9 to Tab. 17 report the results of the experiments by varying the compression ratio of JPEG AI for each detector on every single dataset. For all tables, as commonly done in deepfake detection tasks, we evaluate the BA, FPR, and FNR at the 0 threshold.

**Comparison with standard JPEG.** Tab. 18 to Tab. 26 report the results of the experiments varying the quality factor of JPEG for each detector on every single dataset. For all tables, as commonly done in deepfake detection tasks, we evaluate the BA, FPR, and FNR at the 0 threshold.

## 10. Image splicing localization additional results

Fig. 14 to Fig. 17 report some examples of output maps  $\tilde{M}$  for the TruFor and MMFusion detectors. In all plots, the detectors process the same DSO1 input image compressed with different JPEG AI BPP.

As we reported in Sec. 5 of the main paper, decreasing

the JPEG AI compression ratio degrades the quality of the maps  $\tilde{M}$ . All detectors do not correctly identify all the manipulated pixels in the tampered with area, while flagging many pristine pixels as manipulated. Whenever the BPP values go over 1.0, the output maps tend to match more closely the ones obtained when processing samples in their original format. This is the case, for instance, of Fig. 14.

However, it is interesting to notice that, for certain samples, increasing the BPP during compression does not lead to a better  $\tilde{M}$ . For example, the output of MMFusion in Fig. 16 maintains a high number of false positives even for BPP = 1.0 and BPP = 2.0, and TruFor shows a similar behavior in Fig. 17. Therefore, while the overall tendency highlighted in Tab. 5 is clear, these examples seem to suggest that there is no guarantee that compressing images with high BPP values will not interfere with the responses of the detectors.

## 11. Double JPEG AI compression

The study field relative to multiple JPEG compression is lively [73]. Therefore, in the following, we briefly analyze some of the implications of double JPEG AI compression. Please notice that this analysis is not exhaustive, and we plan to explore the more profound implications of double JPEG AI in future studies.

**Deepfake image detection.** Fig. 18 reports the scores of the [42] detector extracted from pristine images compressed in the scenarios illustrated in Sec. 5.3, namely i) single JPEG AI compression, ii) double JPEG AI compression where the original-format images have been first compressed with the lowest BPP considered, i.e., BPP= 0.12, and then re-compressed at various BPP values, and iii) the original-format images have been first compressed with the highest BPP considered, i.e., BPP= 2.0, and then re-compressed at various BPP values.

Fig. 18b reports the results for the first scenario. As we can quickly inspect, regardless of the BPP value used in the second compression, the scores distribution of pristine samples will lie above the 0 threshold in the area corresponding to the scores distribution of single compressed 0.12 BPP images. On the contrary, Fig. 18c shows that if we first compress the samples with a high BPP value, the distribution of the scores will move accordingly to the BPP value of the second compression operation, i.e., a 0.12 BPP after a 2.0 BPP compression will shift the scores in the same area as a single 0.12 BPP compression. These results suggest that JPEG AI behaves similarly to standard compression formats in the sense that, if a strong compression has been applied to the input samples, the compressed images will likely still bear forensic artifacts relative to the first compression stage regardless of the BPP used in the second one.

**Image splicing localization.** In image splicing localization, the double compression usually does not interest the whole

Table 8. JPEG AI Call For Evidence [1] quality metrics for our dataset of JPEG AI images. For clarity’s sake, we abbreviate the metrics as follows: FSIM as FS, MS-SSIM as MS, NLP as NL, VIF as VI, and VMAF as VF.

Dataset	BPP = 0.12		BPP = 0.25		BPP = 0.5		BPP = 0.75		BPP = 1.0		BPP = 2.0		
	FS / MS / NL / VI / VF	FS / MS / NL / VI / VF	FS / MS / NL / VI / VF	FS / MS / NL / VI / VF	FS / MS / NL / VI / VF	FS / MS / NL / VI / VF	FS / MS / NL / VI / VF	FS / MS / NL / VI / VF	FS / MS / NL / VI / VF	FS / MS / NL / VI / VF	FS / MS / NL / VI / VF	FS / MS / NL / VI / VF	
Imagenet	36.57/0.96/0.42/36.27/76.65	38.36/0.98/0.54/38.00/83.71	40.63/0.99/0.64/39.90/88.92	42.30/1.00/0.69/41.28/91.25	43.55/1.00/0.74/42.32/92.71	46.44/1.00/0.83/44.92/95.25							
COCO	35.41/0.95/0.37/35.13/73.91	36.95/0.98/0.48/36.69/81.23	38.76/0.99/0.58/38.36/87.13	40.21/0.99/0.64/39.32/89.65	41.42/1.00/0.68/40.41/91.26	44.00/1.00/0.78/42.64/94.26							
FFHQ	41.65/0.98/0.52/42.61/86.91	44.06/0.99/0.63/44.61/91.37	47.31/0.99/0.72/46.96/93.27	48.39/1.00/0.79/47.96/95.35	49.66/1.00/0.84/49.21/96.11	52.37/1.00/0.91/51.65/97.52							
LSUN	37.39/0.96/0.39/36.95/74.96	39.25/0.98/0.49/38.76/81.61	42.26/0.99/0.60/41.32/87.69	43.79/0.99/0.65/42.51/89.92	45.43/1.00/0.69/43.82/91.55	48.92/1.00/0.79/47.39/94.39							
RAISE	39.27/0.96/0.40/37.50/78.93	41.04/0.98/0.52/39.35/85.44	42.78/0.97/0.52/40.38/83.17	44.87/1.00/0.69/42.71/92.39	46.01/1.00/0.73/43.69/93.67	48.95/1.00/0.80/46.62/95.67							
LAION	39.82/0.98/0.50/39.83/82.71	42.06/0.99/0.61/42.08/88.74	45.47/1.00/0.71/44.76/92.64	47.93/1.00/0.77/46.76/94.39	49.56/1.00/0.81/47.99/95.42	53.63/1.00/0.87/52.01/96.79							
CelebA	38.64/0.98/0.58/39.76/85.49	41.63/0.99/0.72/42.45/91.35	46.28/1.00/0.81/45.62/94.37	48.52/1.00/0.86/47.75/95.86	50.56/1.00/0.90/49.81/96.67	54.28/1.00/0.95/53.33/97.86							

Table 9. AUC, BA, FPR, and FNR for JPEG AI compression scenario for the [88]-A detector.

Original format	BPP = 0.12		BPP = 0.25		BPP = 0.5		BPP = 0.75		BPP = 1.0		BPP = 2.0	
	AUC / BA / FPR / FNR	AUC / BA / FPR / FNR	AUC / BA / FPR / FNR	AUC / BA / FPR / FNR	AUC / BA / FPR / FNR	AUC / BA / FPR / FNR	AUC / BA / FPR / FNR					
Imagenet	0.88 / 0.70/0.07/0.53	0.58 / 0.55/0.59/0.32	0.66 / 0.61/0.46/0.33	0.73 / 0.66/0.24/0.45	0.78 / 0.68/0.17/0.48	0.81 / 0.68/0.11/0.54	0.86/0.64/0.04/ 0.68					
COCO	0.92 / 0.79/0.07/0.35	0.78 / 0.67/0.52/0.15	0.83 / 0.73/0.41/0.14	0.89 / 0.81/0.17/0.20	0.92 / 0.84/0.10/0.23	0.92 / 0.82/0.10/0.26	0.93/0.75/0.04/ 0.46					
CelebA	0.98 / 0.92/0.03/0.13	0.71 / 0.62/0.59/0.16	0.86 / 0.78/0.25/0.19	0.90 / 0.81/0.11/0.27	0.96 / 0.87/0.03/0.24	0.95 / 0.83/0.02/0.33	0.96/0.82/0.01/ 0.34					
LSUN	0.99 / 0.89/0.00/0.22	0.72 / 0.63/0.55/0.19	0.83 / 0.75/0.27/0.23	0.88 / 0.78/0.10/0.34	0.93 / 0.81/0.05/0.33	0.95 / 0.82/0.02/0.34	0.98/0.80/0.00/ 0.40					

image. Indeed, it is rather common that only the spliced area indicated by the tampering mask  $M$  presents artifacts relative to a previous compression operation. This is because the source and target samples might have been saved with different formats or the same coding scheme but with one of the two images being processed with a more aggressive configuration.

We replicated this scenario by taking a spliced sample from an uncompressed dataset, i.e., DSO-1, and compressing this sample with all the BPP values considered in our experiments. After that, we created several spliced images where the spliced area was JPEG AI compressed at various BPP, and the surrounding content was uncompressed. We finally re-compressed all these images with BPP equal to 0.12 and 2.0. In this way, we are creating a mismatch in the spatial distribution of compression traces due to the spliced area bearing traces of the first JPEG AI compression, similar to the scenario analyzed in double JPEG compression.

Fig. 19 and Fig. 20 report the results of our double JPEG AI splicing operation together with the mask estimated by MMFusion. We also include the results of single-compressing the original format spliced image for reference. As we can quickly inspect, we can draw similar conclusions to the deepfake image detection experiments. In Fig. 20, the images were saved with BPP= 2.0, i.e., with very high quality. In this scenario, if the spliced area has been initially compressed with low BPP, MMFusion can detect this inconsistency and localize the spliced area with results much better than the reference single 2.0 BPP JPEG AI compression. On the other hand, in Fig. 19, the second compression stage at BPP= 0.12 likely erases all the traces relative to the first, hence making MMFusion deliver results very similar to a single JPEG AI compression. These results suggest that the inconsistency in the spatial distribution of JPEG AI artifacts might become a very powerful forensic instrument.

Table 10. AUC, BA, FPR, and FNR for JPEG AI compression scenario for the [88]-B detector.

Original format	BPP = 0.12	BPP = 0.25	BPP = 0.5	BPP = 0.75	BPP = 1.0	BPP = 2.0	
AUC / BA / FPR / FNR							
Imagenet	0.90/ 0.59/0.01/0.81	0.62/ 0.58/0.22/0.61	0.73/ 0.62/0.09/0.67	0.82/ 0.61/0.03/0.74	0.86/ 0.62/0.02/0.75	0.88/ 0.61/0.01/0.77	0.90/0.58/0.01/ 0.82
COCO	0.98/ 0.79/0.01/0.41	0.81/ 0.73/0.17/0.37	0.90/ 0.80/0.08/0.32	0.96/ 0.81/0.02/0.35	0.97/ 0.83/0.01/0.33	0.98/ 0.82/0.01/0.35	0.98/0.78/0.00/ 0.43
CelebA	0.95/ 0.81/0.01/0.37	0.71/ 0.60/0.06/0.74	0.83/ 0.62/0.02/0.74	0.90/ 0.71/0.01/0.56	0.93/ 0.74/0.01/0.50	0.93/ 0.76/0.01/0.48	0.94/0.76/0.00/ 0.48
LSUN	0.98/ 0.77/0.00/0.46	0.71/ 0.66/0.17/0.51	0.83/ 0.71/0.05/0.53	0.90/ 0.71/0.01/0.58	0.94/ 0.74/0.00/0.52	0.96/ 0.74/0.00/0.52	0.98/0.73/0.00/ 0.53

Table 11. AUC, BA, FPR, and FNR for JPEG AI compression scenario for the [42] detector.

Original format	BPP = 0.12	BPP = 0.25	BPP = 0.5	BPP = 0.75	BPP = 1.0	BPP = 2.0	
AUC / BA / FPR / FNR							
Imagenet	0.89/ 0.68/0.01/0.64	0.45/ 0.48/0.95/0.09	0.51/ 0.47/0.83/0.23	0.72/ 0.66/0.36/0.32	0.80/ 0.70/0.14/0.45	0.84/ 0.70/0.06/0.54	0.89/0.68/0.01/ 0.64
COCO	0.96/ 0.67/0.01/0.66	0.56/ 0.52/0.94/0.02	0.68/ 0.55/0.82/0.07	0.83/ 0.74/0.33/0.20	0.89/ 0.77/0.08/0.39	0.90/ 0.73/0.04/0.50	0.95/0.67/0.01/ 0.65
FFHQ	0.93/ 0.80/0.06/0.33	0.58/ 0.50/0.99/0.00	0.56/ 0.52/0.94/0.02	0.81/ 0.76/0.44/0.04	0.75/ 0.70/0.45/0.14	0.91/ 0.84/0.15/0.18	0.88/0.72/0.06/ 0.50

Table 12. AUC, BA, FPR, and FNR for JPEG AI compression scenario for the [32] detector.

Original format	BPP = 0.12	BPP = 0.25	BPP = 0.5	BPP = 0.75	BPP = 1.0	BPP = 2.0	
AUC / BA / FPR / FNR							
Imagenet	0.87/ 0.70/0.01/0.59	0.48/ 0.50/0.99/0.01	0.55/ 0.52/0.66/0.31	0.69/ 0.64/0.05/0.68	0.77/ 0.66/0.01/0.67	0.81/ 0.67/0.01/0.65	0.85/0.68/0.01/ 0.63
COCO	0.96/ 0.74/0.00/0.52	0.47/ 0.49/0.99/0.03	0.69/ 0.58/0.59/0.24	0.80/ 0.74/0.02/0.50	0.87/ 0.72/0.00/0.55	0.91/ 0.72/0.00/0.57	0.95/0.72/0.00/ 0.56
FFHQ	0.89/ 0.87/0.00/0.27	0.79/ 0.52/0.93/0.03	0.75/ 0.68/0.32/0.32	0.84/ 0.58/0.02/0.82	0.84/ 0.62/0.00/0.76	0.89/ 0.67/0.00/0.66	0.90/0.75/0.00/ 0.51

Table 13. AUC, BA, FPR, and FNR for JPEG AI compression scenario for the [70] detector.

Original format	BPP = 0.12	BPP = 0.25	BPP = 0.5	BPP = 0.75	BPP = 1.0	BPP = 2.0	
AUC / BA / FPR / FNR							
Imagenet	0.99/ 0.95/0.02/0.08	0.73/ 0.66/0.49/0.19	0.85/ 0.77/0.23/0.23	0.92/ 0.82/0.09/0.27	0.94/ 0.84/0.06/0.25	0.96/ 0.87/0.04/0.22	0.97/0.90/0.03/ 0.18
COCO	1.00/ 0.99/0.01/0.00	0.88/ 0.71/0.54/0.03	0.95/ 0.83/0.30/0.04	0.99/ 0.94/0.09/0.03	1.00/ 0.97/0.05/0.02	1.00/ 0.97/0.05/0.01	1.00/0.99/0.01/ 0.01
CelebA	0.99/ 0.96/0.07/0.02	0.91/ 0.82/0.30/0.07	0.96/ 0.89/0.12/0.09	0.97/ 0.91/0.11/0.06	0.98/ 0.93/0.09/0.04	0.98/ 0.93/0.10/0.04	0.98/0.93/0.08/ 0.05
LSUN	0.98/ 0.84/0.00/0.32	0.72/ 0.65/0.41/0.28	0.84/ 0.74/0.16/0.36	0.90/ 0.76/0.06/0.42	0.94/ 0.80/0.03/0.37	0.96/ 0.81/0.02/0.37	0.96/0.79/0.01/ 0.41
LAION	0.96/ 0.82/0.01/0.35	0.77/ 0.69/0.34/0.28	0.86/ 0.77/0.12/0.35	0.89/ 0.76/0.05/0.43	0.91/ 0.78/0.03/0.41	0.93/ 0.79/0.02/0.41	0.94/0.80/0.01/ 0.40

Table 14. AUC, BA, FPR, and FNR for JPEG AI compression scenario for the [34]-A detector.

Original format	BPP = 0.12	BPP = 0.25	BPP = 0.5	BPP = 0.75	BPP = 1.0	BPP = 2.0	
AUC / BA / FPR / FNR							
Imagenet	0.90/ 0.70/0.57/0.04	0.59/ 0.50/0.99/0.00	0.69/ 0.52/0.94/0.01	0.75/ 0.56/0.87/0.02	0.79/ 0.59/0.79/0.02	0.81/ 0.62/0.74/0.03	0.85/0.63/0.71/ 0.03
COCO	0.91/ 0.74/0.44/0.09	0.50/ 0.47/0.99/0.06	0.59/ 0.48/0.95/0.09	0.69/ 0.52/0.86/0.10	0.74/ 0.59/0.75/0.07	0.81/ 0.65/0.63/0.08	0.83/0.67/0.57/ 0.09
FFHQ	0.96/ 0.90/0.09/0.10	0.95/ 0.90/0.07/0.14	0.96/ 0.91/0.04/0.13	0.94/ 0.88/0.10/0.14	0.95/ 0.90/0.07/0.14	0.95/ 0.90/0.07/0.14	0.97/0.91/0.06/ 0.11
LSUN	0.95/ 0.87/0.18/0.09	0.50/ 0.51/0.99/0.00	0.52/ 0.52/0.94/0.02	0.59/ 0.52/0.87/0.09	0.65/ 0.55/0.81/0.10	0.64/ 0.54/0.81/0.12	0.81/0.64/0.68/ 0.04
LAION	0.96/ 0.80/0.37/0.03	0.52/ 0.50/0.99/0.01	0.64/ 0.51/0.97/0.01	0.73/ 0.54/0.91/0.01	0.75/ 0.56/0.87/0.02	0.75/ 0.55/0.89/0.02	0.80/0.57/0.83/ 0.02
RAISE	0.80/ 0.65/0.11/0.60	0.68/ 0.65/0.23/0.47	0.73/ 0.65/0.11/0.59	0.58/ 0.55/0.25/0.64	0.79/ 0.64/0.09/0.62	0.80/ 0.64/0.10/0.62	0.79/0.64/0.12/ 0.61

Table 15. AUC, BA, FPR, and FNR for JPEG AI compression scenario for the [34]-B detector.

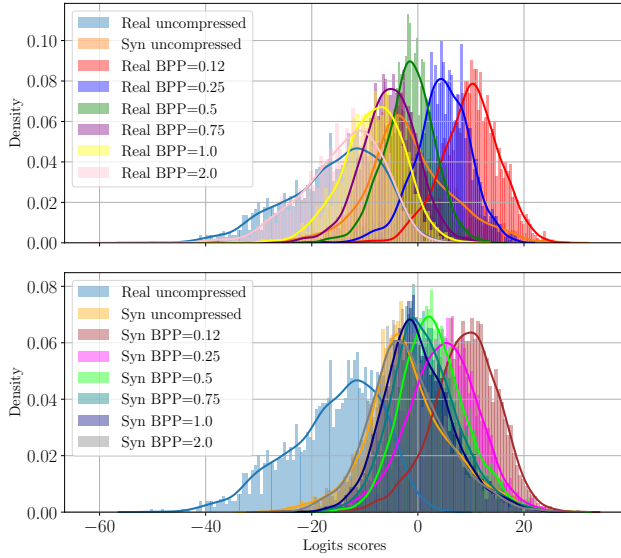
Original format	BPP = 0.12	BPP = 0.25	BPP = 0.5	BPP = 0.75	BPP = 1.0	BPP = 2.0	
AUC / BA / FPR / FNR							
Imagenet	0.76/ 0.68/0.42/0.21	0.61/ 0.51/0.98/0.00	0.68/ 0.53/0.94/0.01	0.71/ 0.55/0.87/0.03	0.72/ 0.57/0.82/0.03	0.74/ 0.59/0.78/0.04	0.75/0.60/0.74/ 0.06
COCO	0.86/ 0.77/0.32/0.14	0.53/ 0.49/0.98/0.04	0.65/ 0.51/0.92/0.06	0.73/ 0.55/0.83/0.08	0.77/ 0.58/0.76/0.07	0.80/ 0.62/0.67/0.08	0.83/0.68/0.55/ 0.10
FFHQ	0.88/ 0.77/0.10/0.36	0.96/ 0.86/0.21/0.08	0.96/ 0.88/0.15/0.09	0.95/ 0.88/0.14/0.11	0.94/ 0.87/0.11/0.15	0.94/ 0.87/0.10/0.17	0.95/0.89/0.09/ 0.14
LSUN	0.79/ 0.68/0.49/0.14	0.52/ 0.51/0.98/0.01	0.56/ 0.52/0.93/0.03	0.62/ 0.53/0.85/0.08	0.67/ 0.55/0.80/0.09	0.66/ 0.55/0.79/0.11	0.72/0.59/0.73/ 0.08
RAISE	0.86/ 0.77/0.15/0.31	0.76/ 0.67/0.47/0.20	0.79/ 0.72/0.29/0.27	0.74/ 0.68/0.35/0.29	0.84/ 0.75/0.20/0.29	0.84/ 0.76/0.19/0.29	0.85/0.76/0.17/ 0.32

Table 16. AUC, BA, FPR, and FNR for JPEG AI compression scenario for the [63] detector.

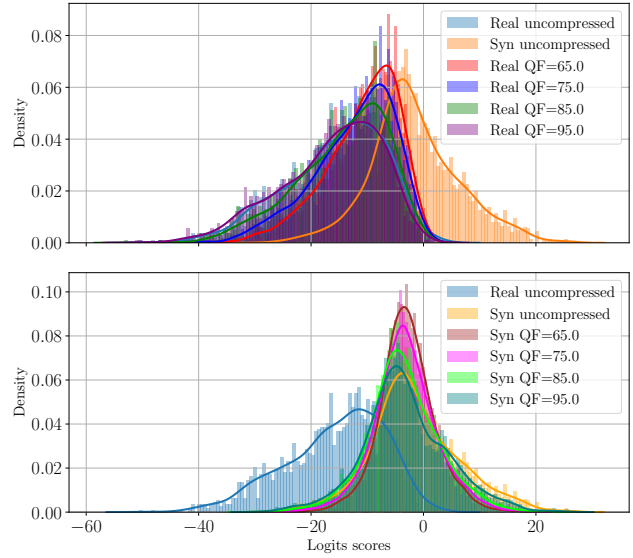
Original format	BPP = 0.12	BPP = 0.25	BPP = 0.5	BPP = 0.75	BPP = 1.0	BPP = 2.0	
AUC / BA / FPR / FNR							
CelebA	1.00/ 1.00/0.00/0.00	0.81/ 0.50/1.00/0.00	0.92/ 0.54/0.93/0.00	0.98/ 0.91/0.18/0.00	1.00/ 0.99/0.02/0.00	1.00/ 0.99/0.01/0.00	1.00/1.00/0.00/ 0.00
FFHQ	1.00/ 1.00/0.00/0.00	0.97/ 0.79/0.39/0.03	0.99/ 0.94/0.07/0.05	1.00/ 0.99/0.00/0.01	1.00/ 1.00/0.00/0.00	1.00/ 1.00/0.00/0.00	1.00/1.00/0.00/ 0.00
Imagenet	0.71/ 0.62/0.13/0.64	0.51/ 0.50/0.72/0.28	0.53/ 0.52/0.50/0.47	0.55/ 0.54/0.39/0.54	0.57/ 0.56/0.33/0.56	0.59/ 0.56/0.28/0.60	0.64/0.59/0.23/ 0.59
LAION	0.72/ 0.68/0.18/0.46	0.61/ 0.59/0.51/0.32	0.63/ 0.60/0.39/0.41	0.69/ 0.63/0.32/0.42	0.72/ 0.66/0.25/0.44	0.73/ 0.67/0.23/0.43	0.73/0.66/0.22/ 0.46
LSUN	0.83/ 0.76/0.12/0.37	0.50/ 0.51/0.82/0.16	0.61/ 0.59/0.55/0.27	0.58/ 0.55/0.50/0.40	0.63/ 0.59/0.38/0.44	0.63/ 0.60/0.32/0.49	0.73/0.68/0.20/ 0.44
RAISE	0.86/ 0.80/0.02/0.38	0.63/ 0.59/0.34/0.48	0.75/ 0.68/0.14/0.51	0.83/ 0.75/0.03/0.48	0.81/ 0.75/0.04/0.46	0.82/ 0.76/0.02/0.46	0.81/0.78/0.03/ 0.42

Table 17. AUC, BA, FPR, and FNR for JPEG AI compression scenario for the [81] detector.

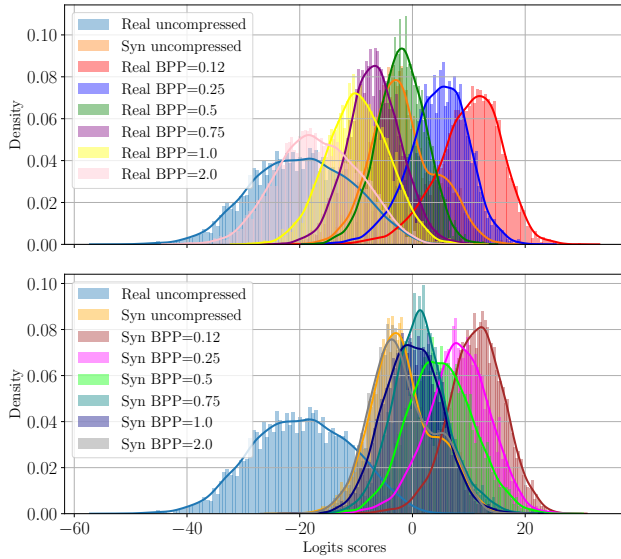
Original format	BPP = 0.12	BPP = 0.25	BPP = 0.5	BPP = 0.75	BPP = 1.0	BPP = 2.0	
AUC / BA / FPR / FNR							
Imagenet	0.94/ 0.84/0.30/0.01	0.50/ 0.51/0.99/0.00	0.46/ 0.51/0.98/0.00	0.44/ 0.51/0.98/0.00	0.46/ 0.51/0.98/0.01	0.47/ 0.51/0.97/0.01	0.52/0.51/0.97/ 0.01
COCO	0.91/ 0.82/0.34/0.01	0.67/ 0.50/1.00/0.00	0.62/ 0.50/0.99/0.00	0.60/ 0.51/0.99/0.00	0.63/ 0.51/0.98/0.00	0.58/ 0.51/0.97/0.00	0.57/0.51/0.97/ 0.00
CelebA	1.00/ 0.99/0.01/0.00	0.67/ 0.50/1.00/0.00	0.74/ 0.50/1.00/0.00	0.60/ 0.50/1.00/0.00	0.81/ 0.50/1.00/0.00	0.77/ 0.50/1.00/0.00	0.92/0.50/1.00/ 0.00
LSUN	1.00/ 0.99/0.00/0.03	0.64/ 0.50/1.00/0.00	0.61/ 0.50/1.00/0.00	0.53/ 0.50/0.99/0.00	0.55/ 0.50/0.99/0.00	0.54/ 0.50/0.99/0.01	0.61/0.51/0.97/ 0.02
LAION	0.99/ 0.97/0.02/0.05	0.80/ 0.51/0.97/0.00	0.75/ 0.51/0.97/0.00	0.75/ 0.52/0.96/0.00	0.74/ 0.52/0.95/0.01	0.79/ 0.53/0.92/0.01	0.82/0.55/0.89/ 0.01



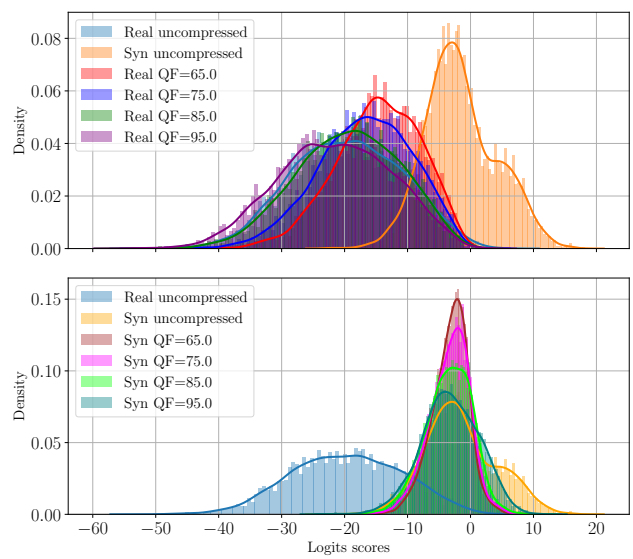
(a) JPEG AI scores distribution over the Imagenet dataset.



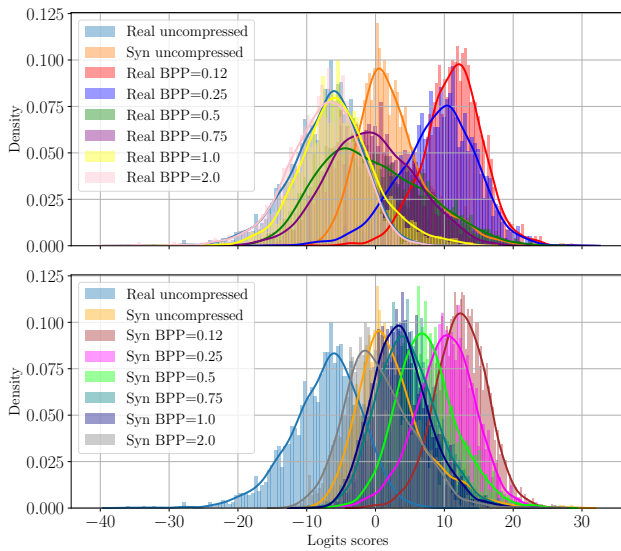
(b) JPEG scores distribution over the Imagenet dataset.



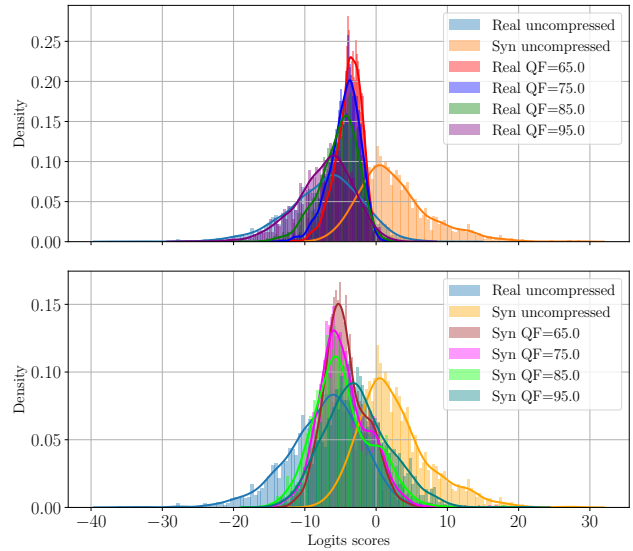
(c) JPEG AI scores distribution over the COCO dataset.



(d) JPEG scores distribution over the COCO dataset.

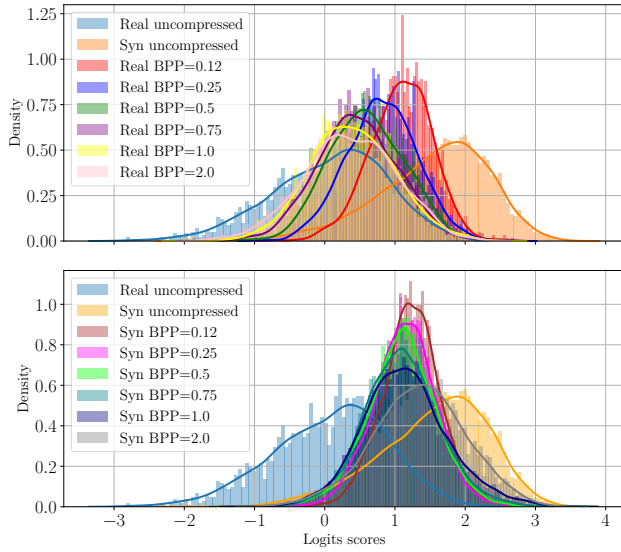


(e) JPEG AI scores distribution over the FFHQ dataset.

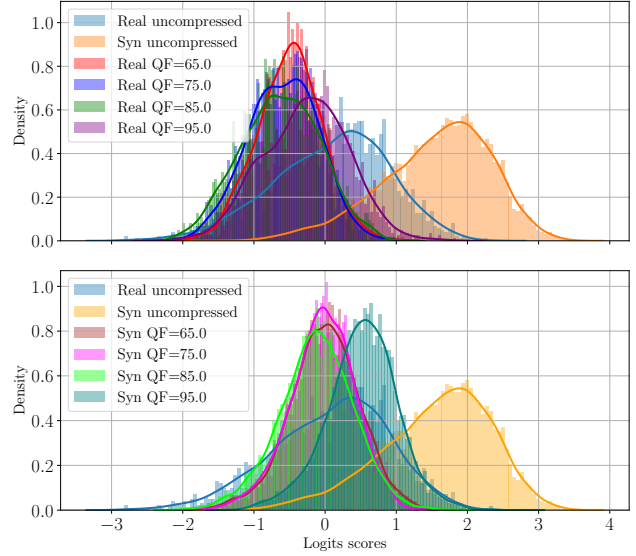


(f) JPEG scores distribution over the FFHQ dataset.

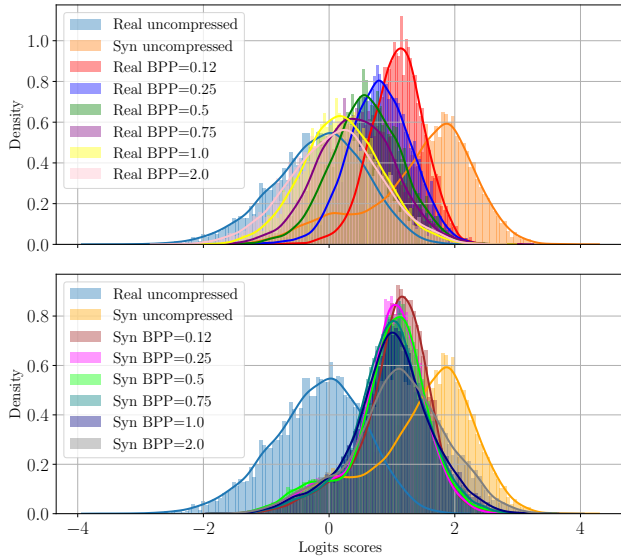
Figure 7. Scores distribution over the different datasets of the [42] detector.



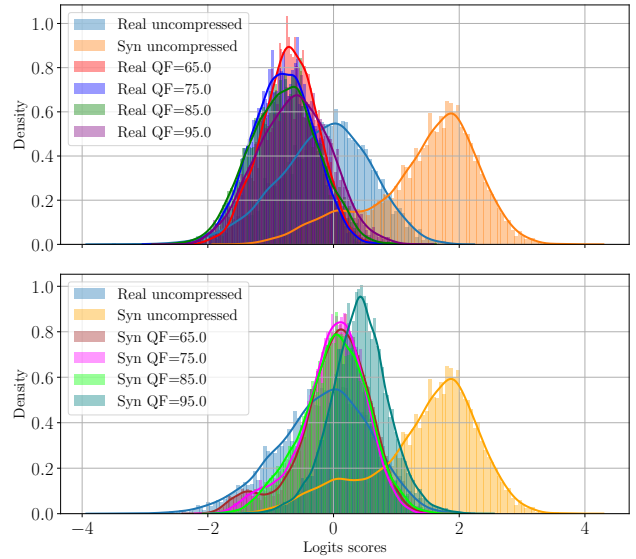
(a) JPEG AI scores distribution over the Imagenet dataset.



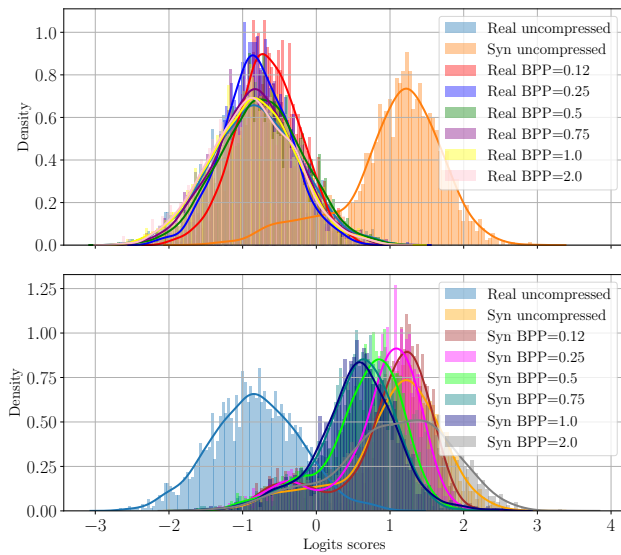
(b) JPEG scores distribution over the Imagenet dataset.



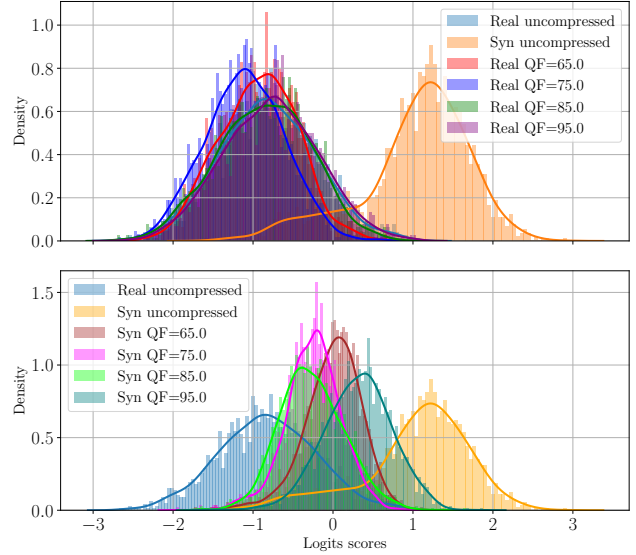
(c) JPEG AI scores distribution over the COCO dataset.



(d) JPEG scores distribution over the COCO dataset.

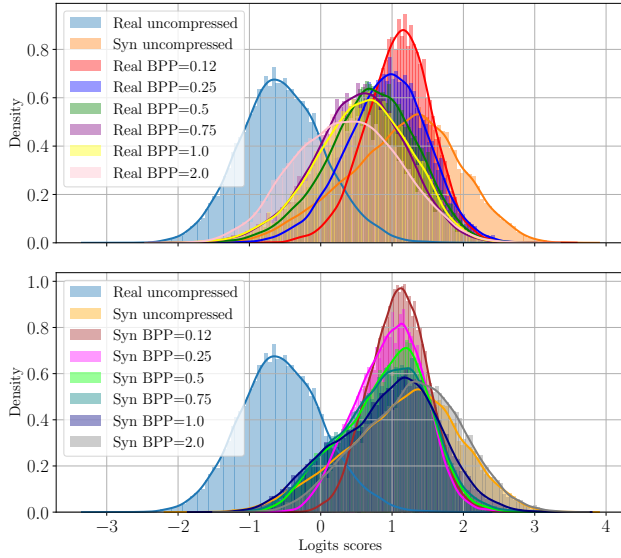


(e) JPEG AI scores distribution over the FFHQ dataset.

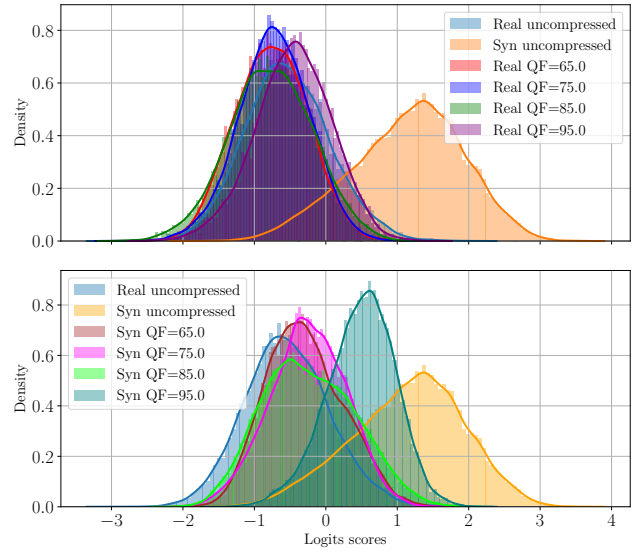


(f) JPEG scores distribution over the FFHQ dataset.

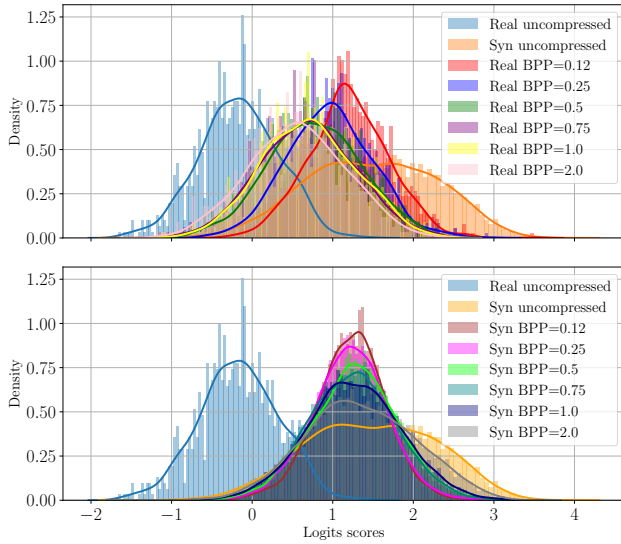
Figure 8. Scores distribution over the ImageNet, COCO, and FFHQ datasets of the [34]-A detector.



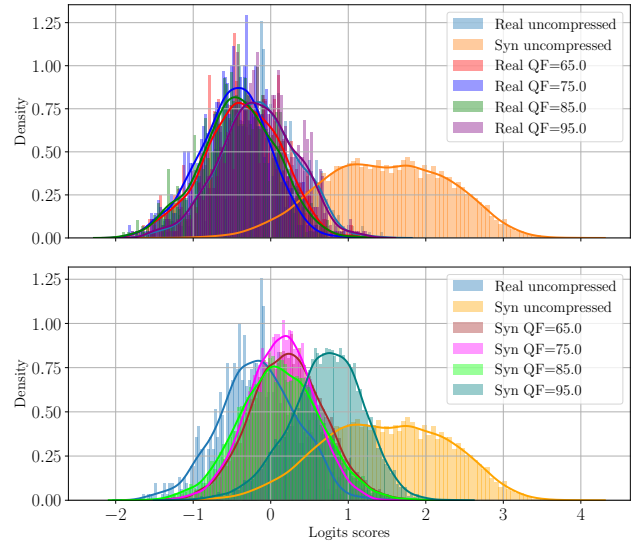
(a) JPEG AI scores distribution over the LSUN dataset.



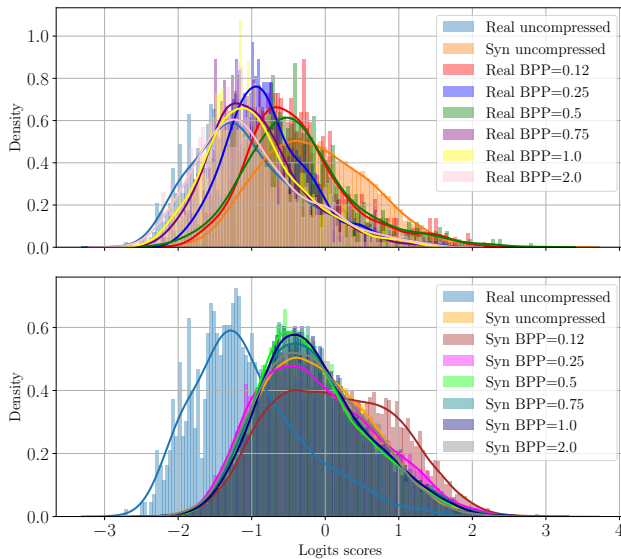
(b) JPEG scores distribution over the LSUN dataset.



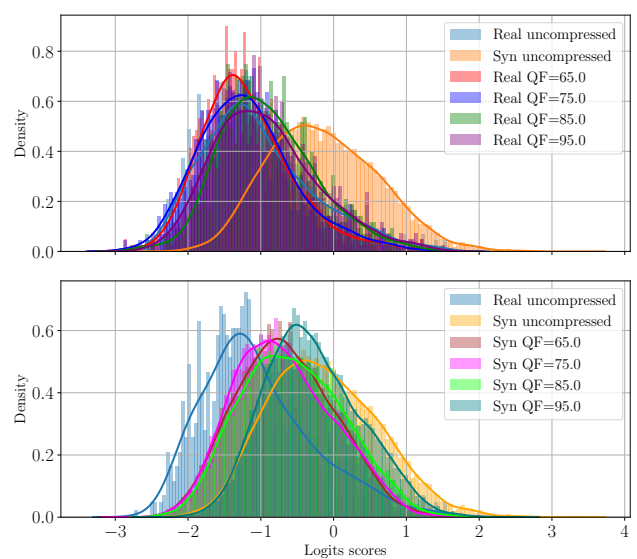
(c) JPEG AI scores distribution over the LAION dataset.



(d) JPEG scores distribution over the LAION dataset.

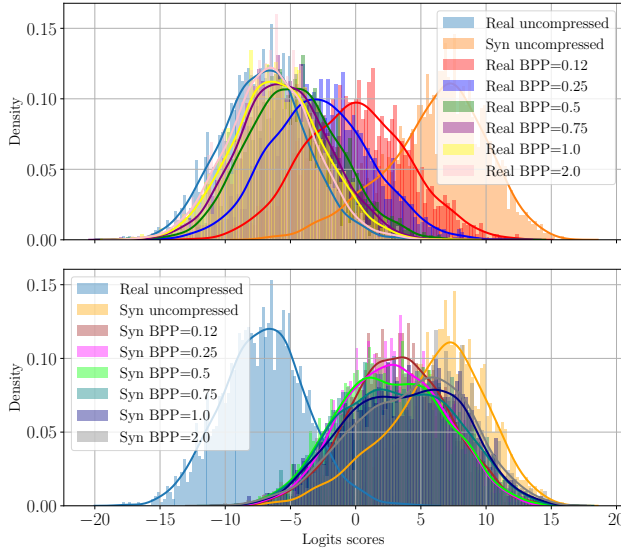


(e) JPEG AI scores distribution over the RAISE dataset.

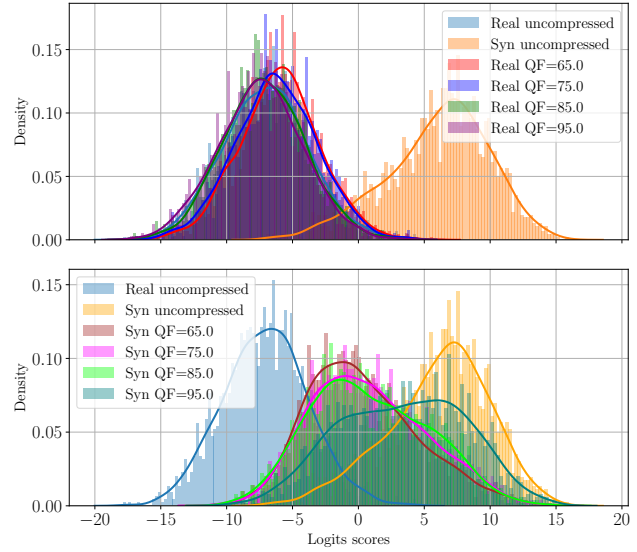


(f) JPEG scores distribution over the RAISE dataset.

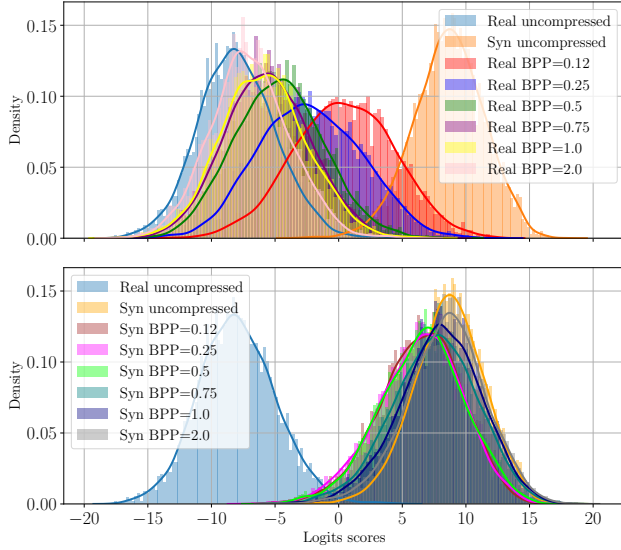
Figure 9. Scores distribution over the LSUN, LAION, and RAISE datasets of the [34]-A detector.



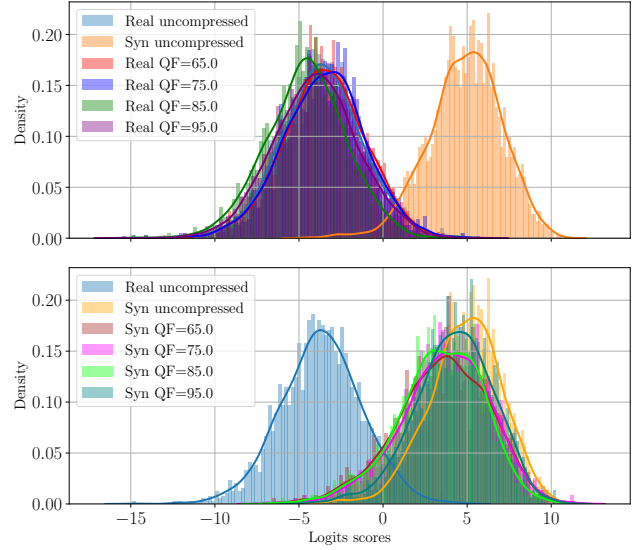
(a) JPEG AI scores distribution over the Imagenet dataset.



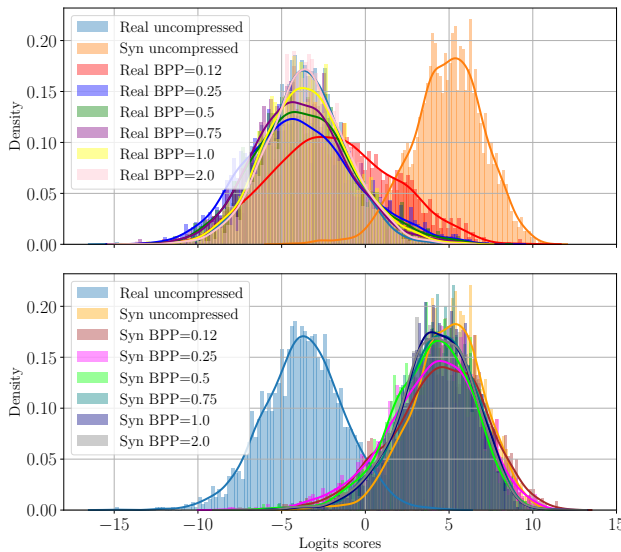
(b) JPEG scores distribution over the Imagenet dataset.



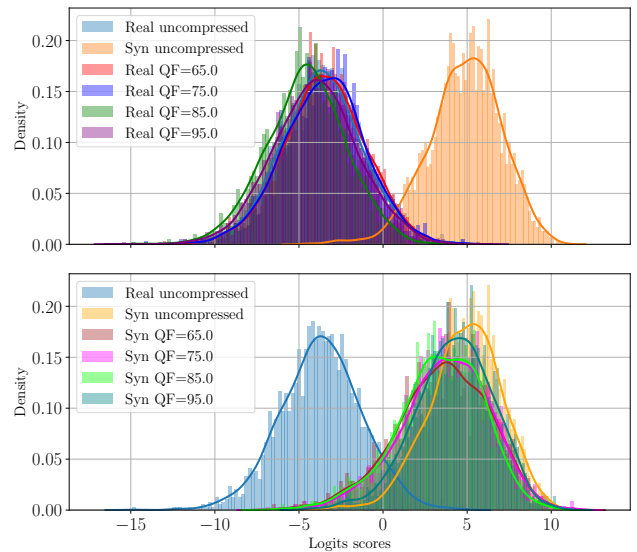
(c) JPEG AI scores distribution over the COCO dataset.



(d) JPEG scores distribution over the COCO dataset.



(e) JPEG AI scores distribution over the CelebA dataset.



(f) JPEG scores distribution over the CelebA dataset.

Figure 10. Scores distribution over the Imagenet, COCO, and CelebA datasets of the [70] detector.

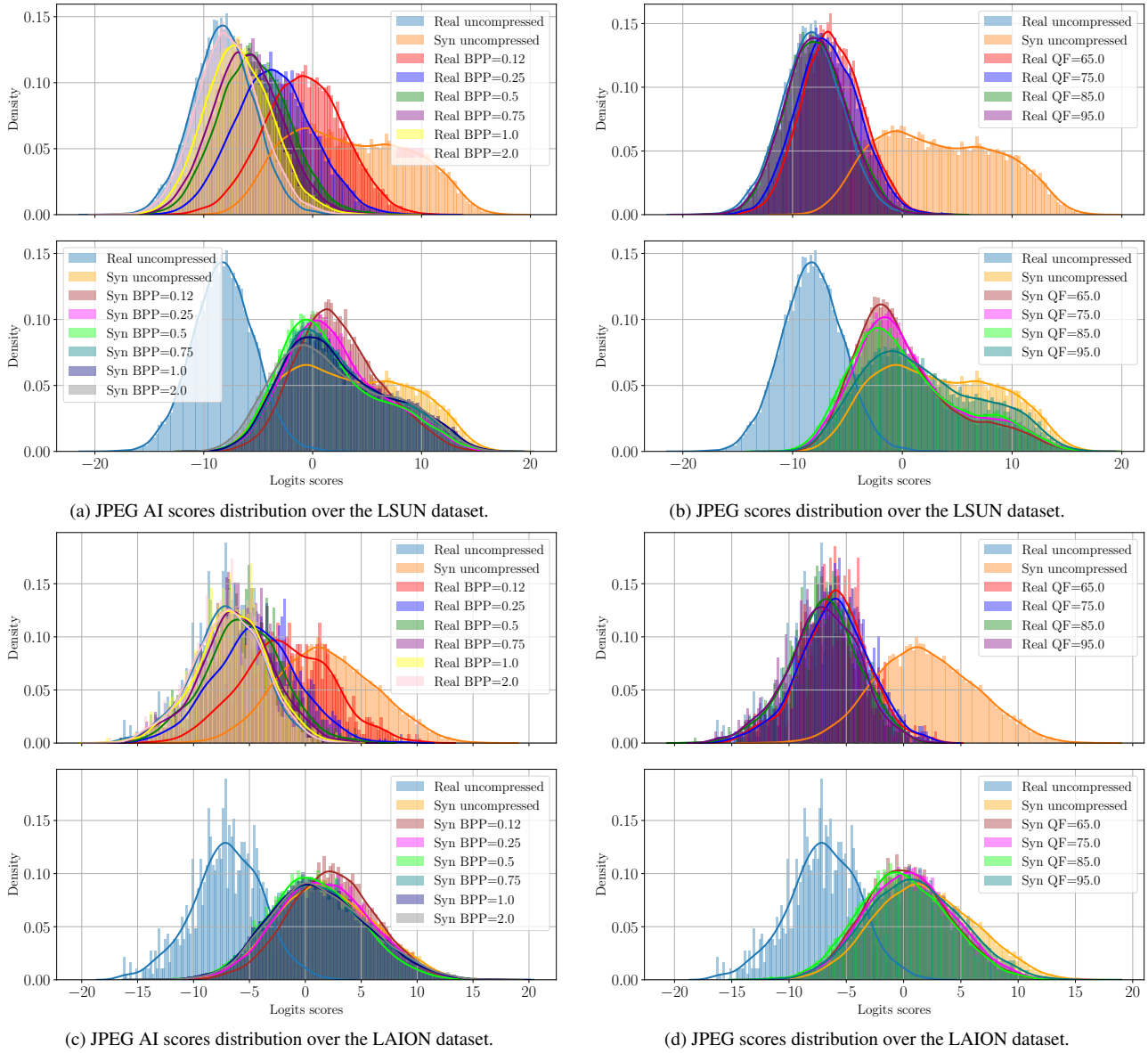
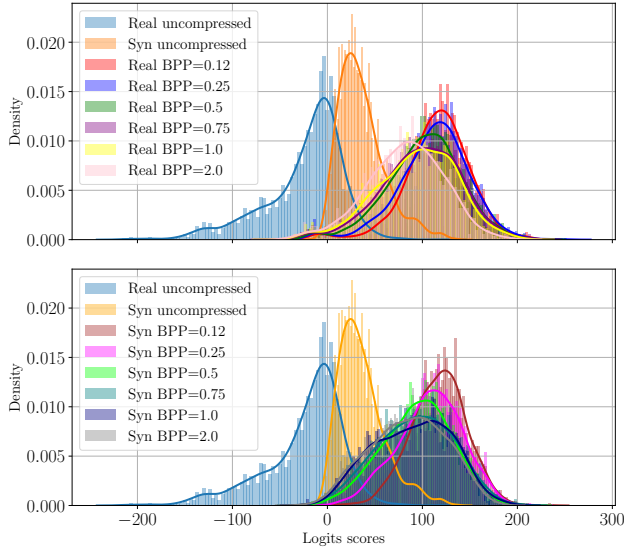


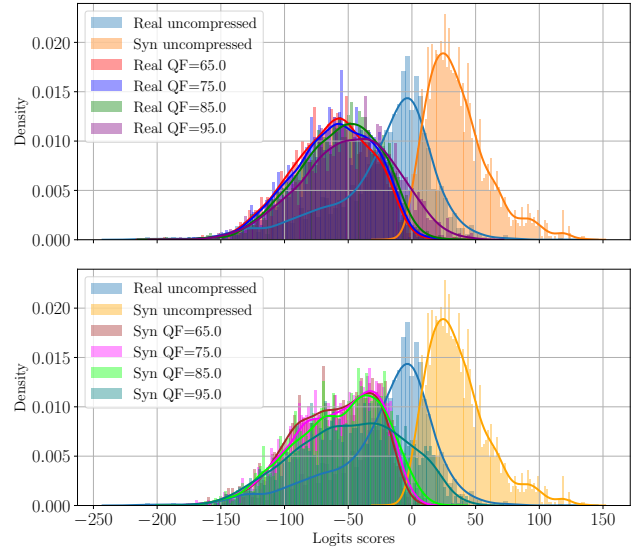
Figure 11. Scores distribution over the LSUN and LAION datasets of the [70] detector.

Table 18. AUC, BA, FPR, and FNR for the JPEG compression scenario for the [88]-A detector.

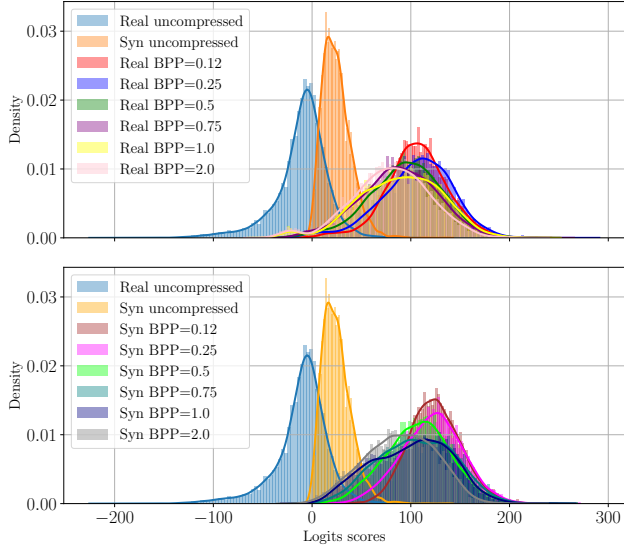
	Original format	QF = 65	BPP = 75	QF = 85	QF = 95
	AUC / BA / FPR / FNR				
Imagenet	0.88/0.70/0.07/0.53	0.88/0.60/0.01/0.79	0.88/0.60/0.01/0.79	0.89/0.60/0.01/0.80	0.89/0.62/0.01/0.74
COCO	0.92/0.79/0.07/0.35	0.96/0.70/0.00/0.59	0.96/0.69/0.00/0.61	0.96/0.68/0.00/0.64	0.96/0.70/0.01/0.60
CelebA	0.98/0.92/0.03/0.13	0.89/0.76/0.04/0.44	0.89/0.75/0.04/0.47	0.91/0.75/0.02/0.47	0.93/0.79/0.02/0.40
LSUN	0.99/0.89/0.00/0.22	0.95/0.72/0.00/0.56	0.96/0.74/0.00/0.53	0.97/0.75/0.00/0.50	0.99/0.79/0.00/0.42



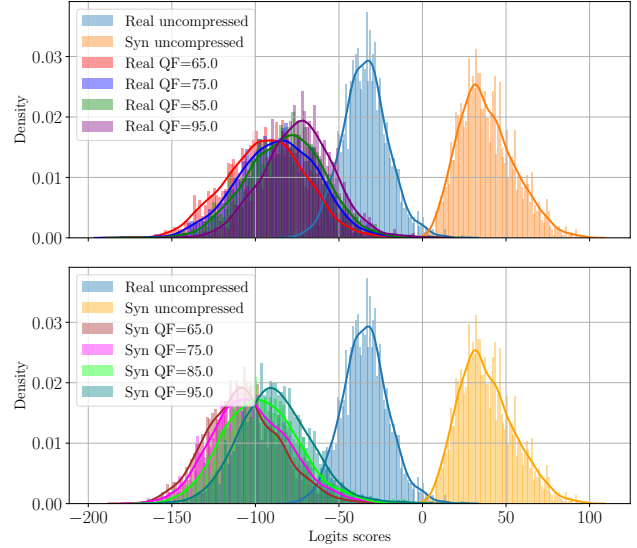
(a) JPEG AI scores distribution over the Imagenet dataset.



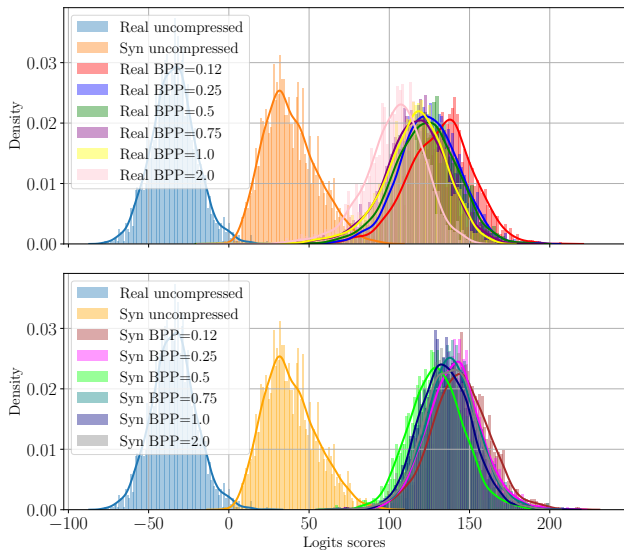
(b) JPEG scores distribution over the Imagenet dataset.



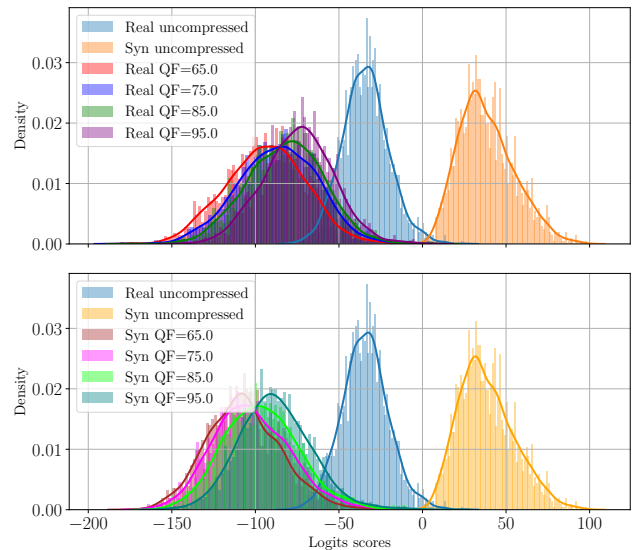
(c) JPEG AI scores distribution over the COCO dataset.



(d) JPEG scores distribution over the COCO dataset.



(e) JPEG AI scores distribution over the CelebA dataset.



(f) JPEG scores distribution over the CelebA dataset.

Figure 12. Scores distribution over the Imagenet, COCO, and CelebA datasets of the [81] detector.

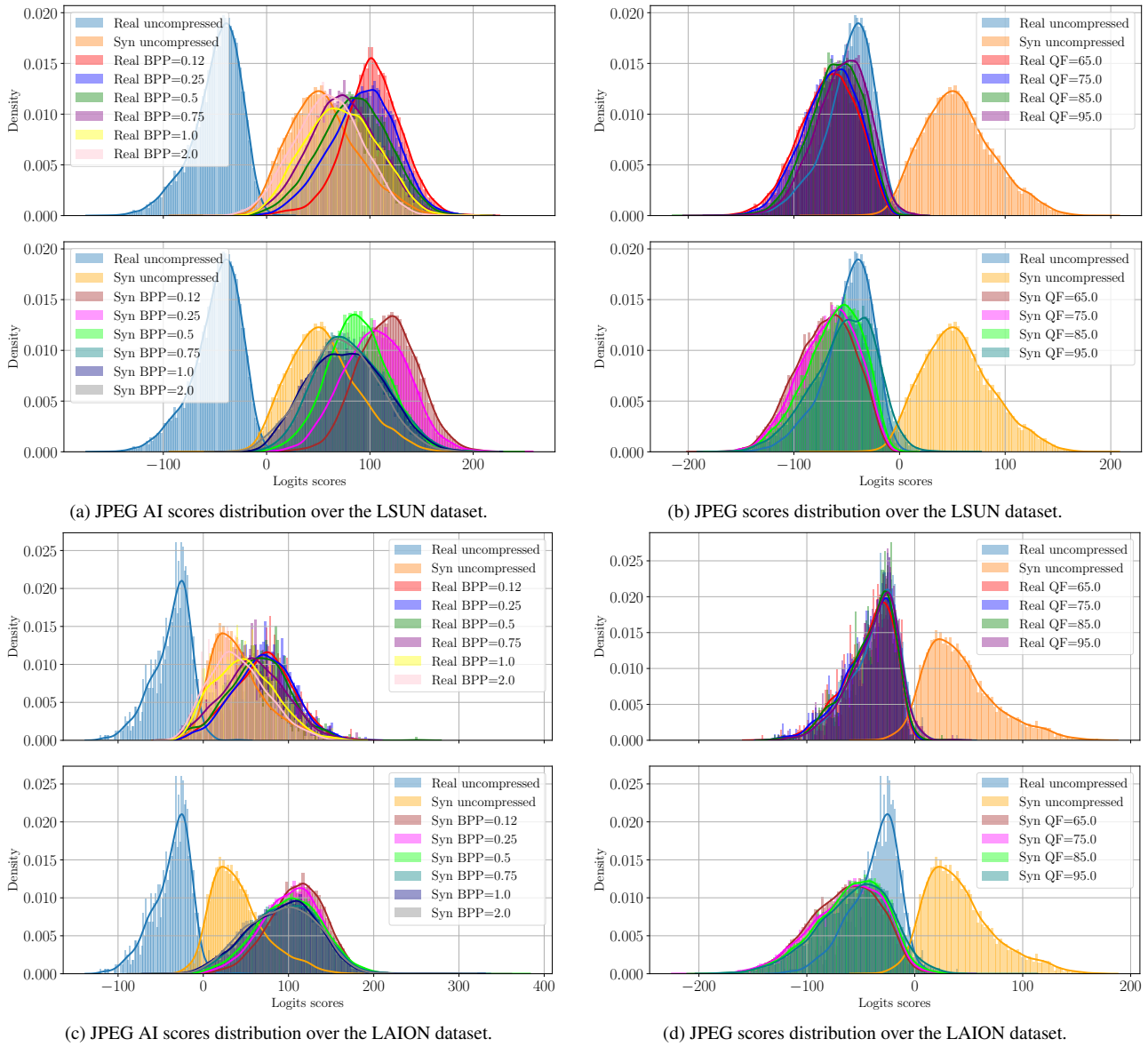


Figure 13. Scores distribution over the LSUN and LAION datasets of the [81] detector.

Table 19. AUC, BA, FPR, and FNR for the JPEG compression scenario for the [88]-B detector.

	Original format	QF = 65	BPP = 75	QF = 85	QF = 95
	AUC / BA / FPR / FNR				
Imagenet	0.90/0.59/0.01/0.81	0.89/0.57/0.01/0.86	0.89/0.57/0.00/0.86	0.90/0.57/0.01/0.86	0.90/0.57/0.01/0.85
COCO	0.98/0.79/0.01/0.41	0.99/0.75/0.00/0.49	0.99/0.75/0.00/0.50	0.99/0.75/0.00/0.51	0.99/0.76/0.00/0.48
CelebA	0.95/0.81/0.01/0.37	0.91/0.73/0.01/0.52	0.92/0.74/0.01/0.50	0.92/0.75/0.01/0.50	0.93/0.76/0.01/0.47
LSUN	0.98/0.77/0.00/0.46	0.96/0.69/0.00/0.61	0.96/0.70/0.00/0.59	0.97/0.71/0.00/0.58	0.98/0.73/0.00/0.54

Table 20. AUC, BA, FPR, and FNR for the JPEG compression scenario for the [42] detector.

Original format	QF = 65	BPP = 75	QF = 85	QF = 95
AUC / BA / FPR / FNR				
Imagenet	0.89/0.68/0.01/0.64	0.84/0.62/0.01/0.76	0.85/0.62/0.01/0.75	0.86/0.63/0.00/0.74
COCO	0.96/0.67/0.01/0.66	0.95/0.55/0.00/0.89	0.96/0.56/0.00/0.87	0.97/0.59/0.00/0.82
FFHQ	0.93/0.80/0.06/0.33	0.42/0.55/0.00/0.91	0.45/0.56/0.00/0.88	0.52/0.58/0.01/0.84

Table 21. AUC, BA, FPR, and FNR for the JPEG compression scenario for the [32] detector.

Original format	QF = 65	BPP = 75	QF = 85	QF = 95
AUC / BA / FPR / FNR				
Imagenet	0.87/0.70/0.01/0.59	0.83/0.72/0.04/0.53	0.83/0.71/0.03/0.56	0.84/0.70/0.01/0.59
COCO	0.96/0.74/0.00/0.52	0.98/0.81/0.00/0.37	0.98/0.79/0.00/0.42	0.98/0.75/0.00/0.50
FFHQ	0.89/0.87/0.00/0.27	0.93/0.81/0.28/0.10	0.93/0.84/0.19/0.13	0.92/0.87/0.06/0.20

Table 22. AUC, BA, FPR, and FNR for the JPEG compression scenario for the [70] detector.

Original format	QF = 65	BPP = 75	QF = 85	QF = 95
AUC / BA / FPR / FNR				
Imagenet	0.99/0.95/0.02/0.08	0.90/0.72/0.03/0.53	0.91/0.75/0.02/0.47	0.94/0.76/0.01/0.46
COCO	1.00/0.99/0.01/0.00	0.99/0.93/0.01/0.13	0.99/0.95/0.01/0.10	1.00/0.96/0.01/0.07
CelebA	0.99/0.96/0.07/0.02	0.97/0.91/0.07/0.10	0.97/0.92/0.07/0.09	0.99/0.94/0.03/0.10
LSUN	0.98/0.84/0.00/0.32	0.91/0.71/0.01/0.58	0.92/0.72/0.01/0.54	0.94/0.72/0.01/0.55
LAION	0.96/0.82/0.01/0.35	0.91/0.75/0.03/0.48	0.91/0.76/0.02/0.45	0.92/0.74/0.01/0.52

Table 23. AUC, BA, FPR, and FNR for the JPEG compression scenario for the [34]-A detector.

Original format	QF = 65	BPP = 75	QF = 85	QF = 95
AUC / BA / FPR / FNR				
Imagenet	0.90/0.70/0.57/0.04	0.77/0.69/0.12/0.50	0.79/0.68/0.11/0.52	0.75/0.64/0.13/0.59
COCO	0.91/0.74/0.44/0.09	0.85/0.75/0.05/0.44	0.87/0.74/0.04/0.47	0.85/0.73/0.08/0.46
FFHQ	0.96/0.90/0.09/0.10	0.94/0.75/0.03/0.46	0.92/0.61/0.01/0.77	0.80/0.60/0.06/0.75
LSUN	0.95/0.87/0.18/0.09	0.73/0.61/0.07/0.72	0.74/0.63/0.07/0.67	0.72/0.63/0.10/0.64
LAION	0.96/0.80/0.37/0.03	0.80/0.71/0.24/0.33	0.84/0.74/0.14/0.37	0.77/0.69/0.21/0.41
RAISE	0.80/0.65/0.11/0.60	0.72/0.56/0.05/0.82	0.71/0.56/0.06/0.82	0.64/0.56/0.10/0.78

Table 24. AUC, BA, FPR, and FNR for the JPEG compression scenario for the [34]-B detector.

Original format	QF = 65	BPP = 75	QF = 85	QF = 95
AUC / BA / FPR / FNR				
Imagenet	0.76/0.68/0.42/0.21	0.66/0.62/0.40/0.36	0.71/0.66/0.36/0.33	0.64/0.60/0.32/0.48
COCO	0.86/0.77/0.32/0.14	0.81/0.73/0.33/0.22	0.86/0.77/0.19/0.26	0.82/0.73/0.17/0.37
FFHQ	0.88/0.77/0.10/0.36	0.87/0.72/0.08/0.47	0.77/0.65/0.18/0.52	0.63/0.54/0.14/0.77
LSUN	0.79/0.68/0.49/0.14	0.70/0.64/0.36/0.35	0.70/0.65/0.39/0.30	0.67/0.62/0.38/0.37
RAISE	0.86/0.77/0.15/0.31	0.78/0.70/0.22/0.37	0.76/0.69/0.21/0.40	0.74/0.68/0.22/0.41

Table 25. AUC, BA, FPR, and FNR for the JPEG compression scenario for the [63] detector.

Original format	QF = 65	BPP = 75	QF = 85	QF = 95
AUC / BA / FPR / FNR				
CelebA	1.00/1.00/0.00/0.00	1.00/1.00/0.01/0.00	1.00/1.00/0.00/0.00	1.00/1.00/0.00/0.00
FFHQ	1.00/1.00/0.00/0.00	1.00/1.00/0.00/0.01	1.00/1.00/0.00/0.00	1.00/1.00/0.00/0.00
Imagenet	0.85/0.78/0.25/0.20	0.58/0.56/0.28/0.60	0.60/0.56/0.30/0.58	0.62/0.59/0.32/0.50
LAION	0.85/0.75/0.32/0.17	0.74/0.66/0.25/0.42	0.73/0.66/0.26/0.41	0.73/0.66/0.30/0.38
LSUN	0.90/0.81/0.23/0.15	0.65/0.61/0.24/0.54	0.66/0.61/0.29/0.49	0.69/0.64/0.32/0.41
RAISE	0.80/0.77/0.15/0.32	0.83/0.76/0.03/0.46	0.85/0.78/0.03/0.41	0.83/0.81/0.04/0.34

Table 26. AUC, BA, FPR, and FNR for the JPEG compression scenario for the [81] detector.

Original format	QF = 65	BPP = 75	QF = 85	QF = 95	
AUC / BA / FPR / FNR					
Imagenet	0.94/0.84/0.30/0.01	0.52/0.50/0.01/1.00	0.52/0.50/0.01/1.00	0.51/0.50/0.01/0.98	0.51/0.53/0.08/0.86
COCO	0.91/0.82/0.34/0.01	0.42/0.50/0.00/1.00	0.42/0.50/0.00/1.00	0.42/0.50/0.00/1.00	0.42/0.49/0.05/0.96
CelebA	1.00/0.99/0.01/0.00	0.34/0.50/0.00/1.00	0.31/0.50/0.00/1.00	0.32/0.50/0.00/1.00	0.31/0.50/0.00/1.00
LSUN	1.00/0.99/0.00/0.03	0.47/0.50/0.00/1.00	0.48/0.50/0.00/1.00	0.49/0.50/0.00/1.00	0.53/0.51/0.01/0.98
LAION	0.99/0.97/0.02/0.05	0.30/0.50/0.00/0.99	0.31/0.50/0.00/0.99	0.33/0.51/0.00/0.99	0.34/0.51/0.02/0.97

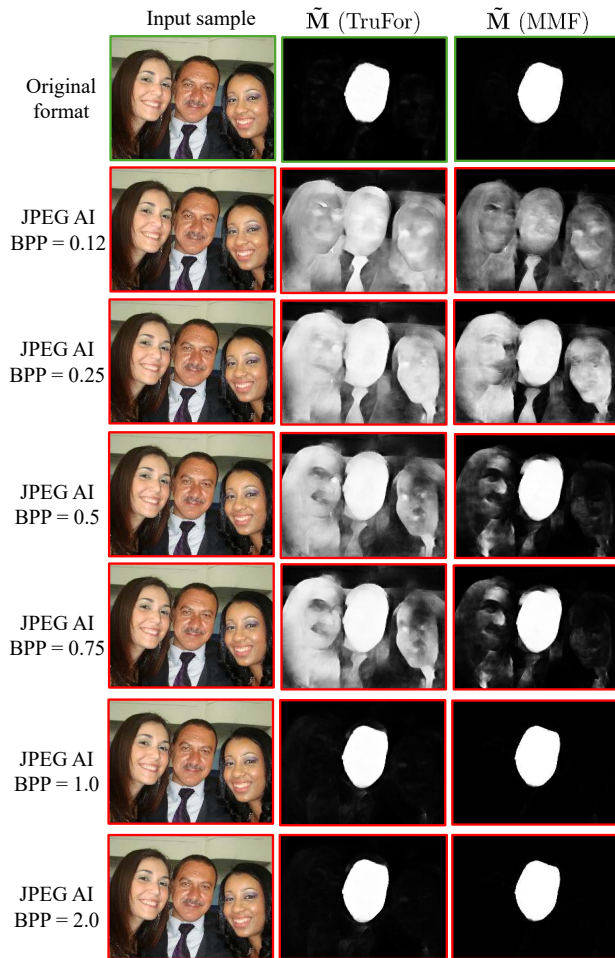


Figure 14. Output of the considered detectors for the same DS01 input under different JPEG AI compression settings.

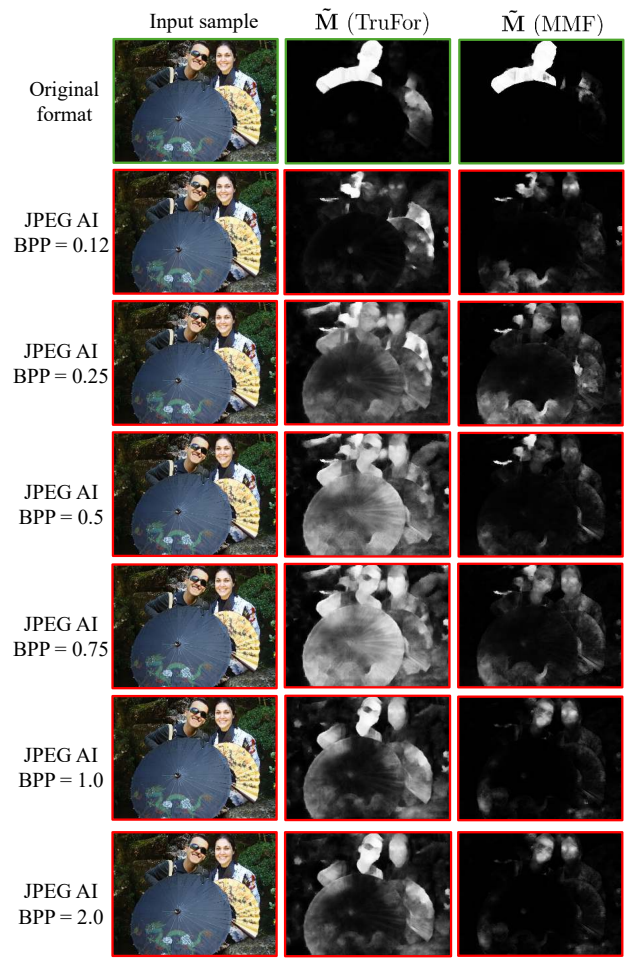


Figure 15. Output of the considered detectors for the same DS01 input under different JPEG AI compression settings.

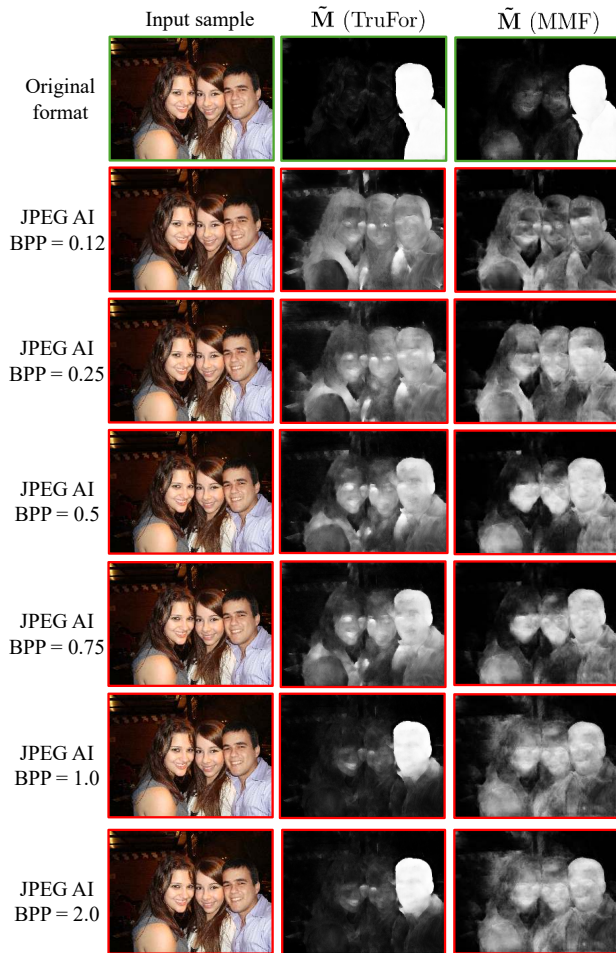
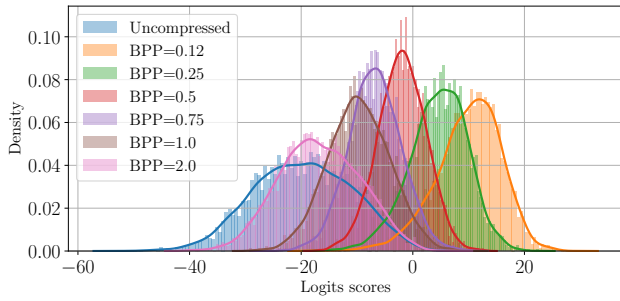


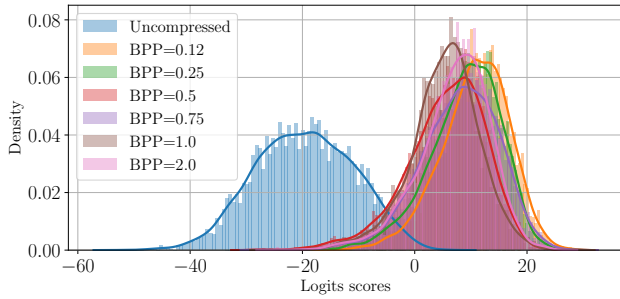
Figure 16. Output of the considered detectors for the same DS01 input under different JPEG AI compression settings.



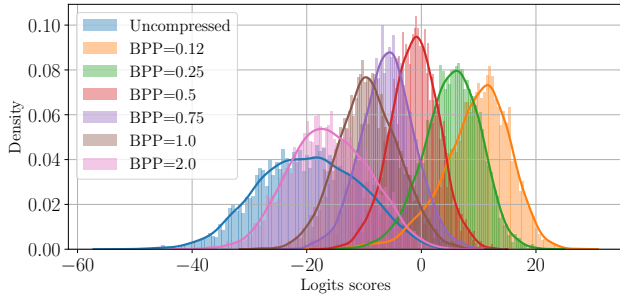
Figure 17. Output of the considered detectors for the same DS01 input under different JPEG AI compression settings.



(a) Single JPEG AI compression.



(b) Double JPEG AI compression, starting BPP= 0.12.



(c) Double JPEG AI compression, starting BPP= 2.0.

Figure 18. Scores distribution over COCO pristine samples of the [42] detector considering different JPEG AI compression stages.



Figure 19. Output of MMFusion for DSO-1 double JPEG AI compressed images. The second compression stage is executed with BPP equal to 0.12. The first compression stage BPP value varies from 0.12 to 2.0 from top to bottom.



Figure 20. Output of MMFusion for DSO-1 double JPEG AI compressed images. The second compression stage is executed with BPP equal to 2.0. The first compression stage BPP value varies from 0.12 to 2.0 from top to bottom.